Tire Characteristics and Vehicle Handling and Stability

Chapter Outline

1.1. INTRODUCTION

This chapter is meant to serve as an introduction to vehicle dynamics with emphasis on the influence of tire properties. Steady-state cornering behavior of simple automobile models and the transient motion after small and large steering inputs and other disturbances will be discussed. The effects of various shape factors of tire characteristics (cf. Figure 1.1) on vehicle handling properties will be analyzed. The slope of the side force F_y vs slip angle α near the origin (the cornering or side slip stiffness) is the determining parameter for the basic linear handling and stability behavior of automobiles. The possible offset of the tire characteristics with respect to their origins may be responsible for the occurrence of the so-called tire-pull phenomenon. The further nonlinear shape of the side (or cornering) force characteristic governs the handling and stability properties of the vehicle at higher lateral accelerations. The load dependency of the curves, notably the nonlinear relationship of cornering stiffness with tire normal load, has a considerable effect on the handling characteristic of the car. For the (quasi)-steady-state handling analysis, simple single track (two-wheel) vehicle models will be used. Front and rear axle effective side force characteristics are introduced to represent effects that result from suspension and steering system design factors such as steering compliance, roll steer, and lateral load transfer. Also, the effect of possibly applied (moderate) braking and driving forces may be incorporated in the effective characteristics. Large braking forces may result in wheel lock and possibly large deviations from the undisturbed path. The motion resulting from wheel lock will be dealt with in an application of the theory of a simple physical tire model in Chapter 3 (the brush model). The application of the handling and stability theory to the dynamics of heavy trucks will also be briefly dealt with in this chapter. Special attention will be given to the phenomenon of oscillatory instability that may show up with the car-trailer combination.
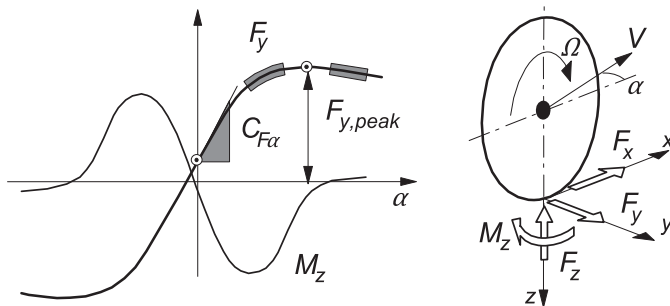

FIGURE 1.1 Characteristic shape factors (indicated by points and shaded areas) of tire or axle characteristics that may influence vehicle handling and stability properties. Slip angle and force and moment positive directions, cf. App. 1.

When the wavelength of an oscillatory motion of the vehicle that may arise from road unevenness, brake torque fluctuations, wheel unbalance, or instability (shimmy) is smaller than say 5 m, a non-steady-state or transient description of tire response is needed to properly analyze the phenomenon. In Chapters 5–8, these matters will be addressed. Applications demonstrate the use of transient and oscillatory tire models and provide insight into the vehicle dynamics involved. Chapter 11 is especially devoted to the analysis of motorcycle cornering behavior and stability.

1.2. TIRE AND AXLE CHARACTERISTICS

Tire characteristics are of crucial importance for the dynamic behavior of the road vehicle. In this section, an introduction is given to the basic aspects of the force- and moment-generating properties of the pneumatic tire. Both the pure and combined slip characteristics of the tire are discussed and typical features presented. Finally, the so-called effective axle characteristics are derived from the individual tire characteristics and the relevant properties of the suspension and steering system.

1.2.1. Introduction to Tire Characteristics

The upright wheel rolling freely, that is without applying a driving torque, over a flat level road surface along a straight line at zero side slip, may be defined as the starting situation with all components of slip equal to zero. A relatively small pulling force is needed to overcome the tire-rolling resistance, and a side force and (self)-aligning torque may occur as a result of the not completely symmetric structure of the tire. When the wheel moves in a way that the condition of zero slip is no longer fulfilled, wheel slip occurs that is accompanied by a buildup of additional tire deformation and possibly partial sliding in the contact patch. As a result, (additional) horizontal forces and the aligning torque are generated. The mechanism responsible for this is treated in detail in the subsequent chapters. For now, we will suffice with some important experimental observations and define the various slip quantities that serve as inputs into the tire system and the moment and forces that are the output quantities (positive directions according to Figure 1.1). Several alternative definitions are in use as well. In Appendix 1, various sign conventions of slip, camber, and output forces and moments together with relevant characteristics have been presented.

For the freely rolling wheel, the forward speed V_x (longitudinal component of the total velocity vector V of the wheel center) and the angular speed of revolution Ω_o can be taken from measurements. By dividing these two quantities, the so-called effective rolling radius r_e is obtained:

$$r_e = \frac{V_x}{\Omega_o} \tag{1.1}$$

Although the effective radius may be defined also for a braked or driven wheel, we restrict the definition to the case of free rolling. When a torque is applied about the wheel spin axis, a longitudinal slip arises that is defined as follows:

$$\kappa = -\frac{V_x - r_e\Omega}{V_x} = -\frac{\Omega_o - \Omega}{\Omega_o} \qquad (1.2)$$

The sign is taken such that for a positive κ, a positive longitudinal force F_x arises, that is, a driving force. In that case, the wheel angular velocity Ω is increased with respect to Ω_o and consequently $\Omega > \Omega_o = V_x/r_e$. During braking, the fore-and-aft slip becomes negative. At wheel lock, obviously, $\kappa = -1$. At driving on slippery roads, κ may attain very large values. To limit the longitudinal slip K to a maximum equal to one, in some texts the longitudinal slip is defined differently in the driving range of slip: in the denominator of (1.2), Ω_o is replaced by Ω. This will not be done in the present text.

Lateral wheel slip is defined as the ratio of the lateral and the forward velocity of the wheel. This corresponds to minus the tangent of the slip angle α (Figure 1.1). Again, the sign of α has been chosen such that the side force becomes positive at positive slip angle.

$$\tan \alpha = -\frac{V_y}{V_x} \qquad (1.3)$$

The third and last slip quantity is the so-called spin which is due to rotation of the wheel about an axis normal to the road. Both the yaw rate resulting in path curvature when α remains zero and the wheel camber or inclination angle γ of the wheel plane about the x axis contribute to the spin. The camber angle is defined to be positive when, if looking from behind the wheel, the wheel is tilted to the right. In Chapter 2, more precise definitions of the three components of wheel slip will be given. The forces F_x and F_y and the aligning torque M_z are results of the input slip. They are functions of the slip components and the wheel load. For steady-state rectilinear motions, we have, in general,

$$F_x = F_x(\kappa, \alpha, \gamma, F_z), \quad F_y = F_y(\kappa, \alpha, \gamma, F_z), \quad M_z = M_z(\kappa, \alpha, \gamma, F_z) \quad (1.4)$$

The vertical load F_z may be considered as a given quantity that results from the normal deflection of the tire. The functions can be obtained from measurements for a given speed of travel and road and environmental conditions.

Figure 1.1 shows the adopted system of axes (x, y, z) with associated positive directions of velocities and forces and moments. The exception is the vertical force F_z acting from road to tire. For practical reasons, this force is defined to be positive in the upward direction and thus equal to the normal load of the tire. Also, Ω (not provided with a y subscript) is defined

positive with respect to the negative *y*-axis. Note that the axes system is in accordance with SAE standards (SAE J670e 1976). The sign of the slip angle, however, is chosen opposite with respect to the SAE definition, cf. Appendix 1.

In Figure 1.2 typical pure lateral ($\kappa = 0$) and longitudinal ($\alpha = 0$) slip characteristics have been depicted together with a number of combined slip curves. The camber angle γ was kept equal to zero. We define pure slip to be the situation when either longitudinal or lateral slip occurs in isolation. The figure indicates that a drop in force arises when the other slip component is added. The resulting situation is designated as combined slip. The decrease in force can be simply explained by realizing that the total horizontal frictional force F cannot exceed the maximum value (radius of 'friction circle') which is dictated by the current friction coefficient and normal load. Later, in Chapter 3 this becomes clear when considering the behavior of a simple physical tire model. The diagrams include the situation when the brake slip ratio has finally attained the value of 100% ($\kappa = -1$) which corresponds to wheel lock.

The slopes of the pure slip curves at vanishing slip are defined as the longitudinal and lateral slip stiffnesses, respectively. The longitudinal slip stiffness is designated as $C_{F\kappa}$. The lateral slip or cornering stiffness of the tire, denoted by $C_{F\alpha}$, is one of the most important property parameters of the tire and is crucial for the vehicle's handling and stability performance. The slope of minus the aligning torque versus slip angle curve (Figure 1.1) at zero slip angle is termed as the aligning stiffness and is denoted by $C_{M\alpha}$. The ratio of minus the aligning torque and the side force is the pneumatic trail *t* (if we neglect the so-called residual torque to be dealt with in Chapter 4). This length is the distance behind the contact center (projection of wheel center onto the ground in wheel plane direction) to the point where the resulting lateral force acts. The linearized force and moment characteristics (valid at small levels of slip) can be
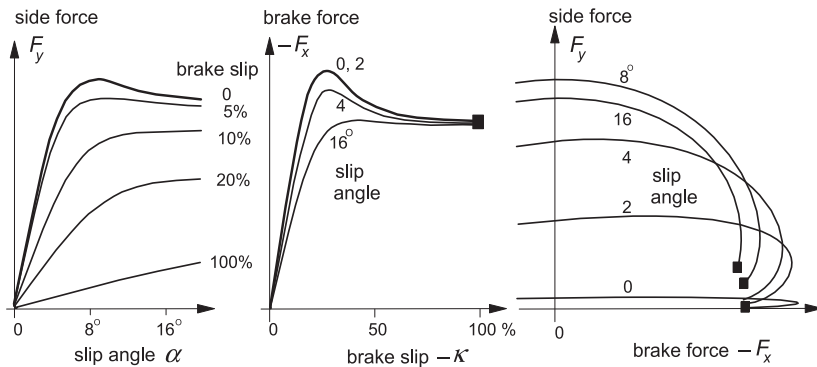

FIGURE 1.2   Combined side force and brake force characteristics.

represented by the following expressions in which the effect of camber has been
included:

$$F_x = C_{F\kappa}\,\kappa$$
$$F_y = C_{F\alpha}\,\alpha + C_{F\gamma}\gamma \tag{1.5}$$
$$M_z = -C_{M\alpha}\,\alpha + C_{M\gamma}\gamma$$

These equations have been arranged in such a way that all the coefficients (the
force, moment slip, and camber stiffnesses) become positive quantities.

It is of interest to note that the order of magnitude of the tire cornering
stiffness ranges from about 6 to about 30 times the vertical wheel load when the
cornering stiffness is expressed as force per radian. The lower value holds for the
older bias-ply tire construction and the larger value for modern racing tires. The
longitudinal slip stiffness has been typically found to be about 50% larger than
the cornering stiffness. The pneumatic trail is approximately equal to a quarter of
the contact patch length. The dry friction coefficient usually equals ca. 0.9 on
very sharp surfaces and ca. 1.6 on clean glass; racing tires may reach 1.5–2.

For the side force which is the more important quantity in connection with
automobile handling properties, a number of interesting diagrams have been
presented in Figure 1.3. These characteristics are typical for truck and car tires
and are based on experiments conducted at the University of Michigan
Transportation Research Institute (UMTRI, formerly HSRI), cf. Ref. (Segel
et al. 1981). The car tire cornering stiffness data stem from newer findings. It is
observed that the cornering stiffness changes in a less than proportional fashion
with the normal wheel load. The maximum normalized side force $F_{y,\mathrm{peak}}/F_z$
appears to decrease with increasing wheel load. Marked differences in level and
slope occur for the car and truck tire curves also when normalized with respect
to the rated or nominal load. The cornering force vs slip angle characteristic
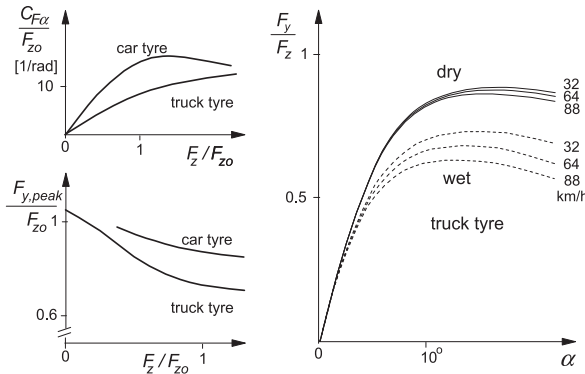shown at different speeds and road conditions indicates that the slope at zero

FIGURE 1.3 Typical characteristics for the normalized cornering stiffness, peak side force, and
side force vs normalized vertical load and slip angle respectively. F_{zo} is the rated load.

slip angle is not or hardly affected by the level of speed and by the wet or dry condition. The peak force level shows only little variation if the road is dry. On a wet road, a more pronounced peak occurs and the peak level drops significantly with increasing speed.

Curves which exhibit a shape like the side force characteristics of Figure 1.3 can be represented by a mathematical formula called *'magic formula'*. A full treatment of the empirical tire model associated with this formula is given in Chapter 4. For now we can suffice with showing the basic expressions for the side force and the cornering stiffness:

$$F_y = D \sin[C \arctan\{B\alpha - E(B\alpha - \arctan(B\alpha))\}]$$

with stiffness factor

$$B = C_{F\alpha}/(CD)$$

peak factor

$$D = \mu F_z (= F_{y,\text{peak}})$$

and cornering stiffness

$$C_{F\alpha}(= BCD) = c_1 \sin\{2 \arctan(F_z/c_2)\}$$

(1.6)

The shape factors C and E as well as the parameters c_1 and c_2 and the friction coefficient μ (possibly depending on the vertical load and speed) may be estimated or determined through regression techniques.

1.2.2. Effective Axle Cornering Characteristics

For the basic analysis of (quasi)-steady-state turning behavior, a simple two-wheel vehicle model may be used successfully. Effects of suspension and steering system kinematics and compliances such as steer compliance, body roll, and also load transfer may be taken into account by using effective axle characteristics. The restriction to (quasi)-steady-state becomes clear when we realize that for transient or oscillatory motions, exhibiting yaw and roll accelerations and differences in phase, variables like roll angle and load transfer can no longer be written as direct algebraic functions of one of the lateral axle forces (front or rear). Consequently, we should drop the simple method of incorporating the effects of a finite center of gravity height if the frequency of input signals such as the steering wheel angle cannot be considered small relative to the body roll natural frequency. Since the natural frequency of the wheel suspension and steering systems is relatively high, the restriction to steady-state motions becomes less critical in the case of the inclusion of e.g., steering compliance in the effective characteristic. Chiesa and Rinonapoli (1967) were among the first to employ effective axle characteristics or 'working curves' as these were referred to by them. Vågstedt (1995) determined these curves experimentally.

Before assessing the complete nonlinear effective axle characteristics, we will first direct our attention to the derivation of the effective cornering

stiffnesses which are used in the simple linear two-wheel model. For these to be determined, a more comprehensive vehicle model has to be defined.

Figure 1.4 depicts a vehicle model with three degrees of freedom. The forward velocity u may be kept constant. As motion variables, we define the lateral velocity v of reference point A, the yaw velocity r, and the roll angle φ. A moving axes system (A, x, y, z) has been introduced. The x-axis points forwards and lies both in the ground plane and in the plane normal to the ground that passes through the so-called roll axis. The y-axis points to the right and the z-axis points downward. This latter axis passes through the center of gravity when the roll angle is equal to zero. In this way, the location of the point of reference A has been defined. The longitudinal distance to the front axle is a and the distance to the rear axle is b. The sum of the two distances is the wheel base l. For convenience, we may write $a = a_1$ and $b = a_2$.

In a curve, the vehicle body rolls about the roll axis. The location and attitude of this virtual axis are defined by the heights $h_{1,2}$ of the front and rear roll centers. The roll axis is assessed by considering the body motion with respect to the four contact centers of the wheels on the ground under the action of an external lateral force that acts on the center of gravity. Due to the symmetry of the vehicle configuration and the linearization of the model, these locations can be considered as fixed. The roll center locations are governed by suspension kinematics and possibly suspension lateral compliances. The torsional springs depicted in the figure represent the front and rear roll stiffnesses $c_{\varphi1,2}$ which result from suspension springs and antiroll bars.
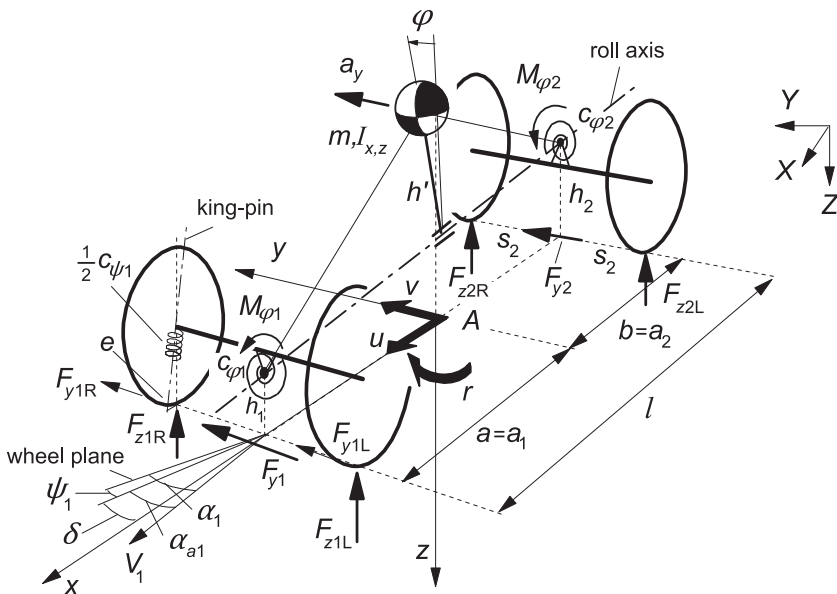

FIGURE 1.4   Vehicle model showing three degrees of freedom: lateral, yaw, and roll.

The fore-and-aft position of the center of gravity of the body is defined by a and b; its height follows from the distance h' to the roll axis. The body mass is denoted by m and the moments of inertia with respect to the center of mass and horizontal and vertical axes by I_x, I_z, and I_{xz}. These latter quantities will be needed in a later phase when the differential equations of motion are established. The unsprung masses will be neglected or they may be included as point masses attached to the roll axis and thus make them part of the sprung mass, that is, the vehicle body.

Furthermore, the model features torsional springs around the steering axes. The king-pin is positioned at a small caster angle that gives rise to the caster length e as indicated in the drawing. The total steering torsional stiffness, left plus right, is denoted by $c_{\psi 1}$.

Effective Axle Cornering Stiffness

Linear analysis, valid for relatively small levels of lateral accelerations, allows the use of approximate tire characteristics represented by just the slopes at zero slip. We will first derive the effective axle cornering stiffness that may be used under these conditions. The effects of load transfer, body roll, steer compliance, side force steer, and initial camber and toe angles will be included in the ultimate expression for the effective axle cornering stiffness.

The linear expressions for the side force and the aligning torque acting on a tire have been given by Eqns (1.5). The coefficients appearing in these expressions are functions of the vertical load. For small variations with respect to the average value (designated with subscript o), we write for the cornering and camber force stiffnesses the linearized expressions:

$$
\begin{aligned}
C_{F\alpha} &= C_{F\alpha o} + \zeta_\alpha \Delta F_z \\
C_{F\gamma} &= C_{F\gamma o} + \zeta_\gamma \Delta F_z
\end{aligned}
\tag{1.7}
$$

where the increment of the wheel vertical load is denoted by ΔF_z and the slopes of the coefficient versus load curves at $F_z = F_{zo}$ are represented by $\zeta_{\alpha,\gamma}$.

When the vehicle moves steadily around a circular path, a centripetal acceleration a_y occurs and a centrifugal force $K = ma_y$ can be said to act on the vehicle body at the center of gravity in the opposite direction. The body roll angle φ that is assumed to be small is calculated by dividing the moment about the roll axis by the apparent roll stiffness which is reduced with the term mgh' due to the additional moment $mgh'\varphi$:

$$
\varphi = \frac{-ma_y h'}{c_{\varphi 1} + c_{\varphi 2} - mgh'}
\tag{1.8}
$$

The total moment about the roll axis is distributed over the front and rear axles in proportion to the front and rear roll stiffnesses. The load transfer ΔF_{zi}

from the inner to the outer wheels that occurs at axle i ($= 1$ or 2) in a steady-state cornering motion with centripetal acceleration a_y follows from the formula:

$$\Delta F_{zi} = \sigma_i m a_y \tag{1.9}$$

with the load transfer coefficient of axle i:

$$\sigma_i = \frac{1}{2 s_i}\left(\frac{c_{\varphi i}}{c_{\varphi 1} + c_{\varphi 2} - mgh'} h' + \frac{l - a_i}{l} h'\right) \tag{1.10}$$

The attitude angle of the roll axis with respect to the horizontal is considered small. In the formula, s_i denotes half the track width, h' is the distance from the center of gravity to the roll axis, and $a_1 = a$ and $a_2 = b$. The resulting vertical loads at axle i for the left (L) and right (R) wheels become, after considering the left and right increments in load,

$$\begin{aligned}
\Delta F_{ziL} &= \Delta F_{zi}, & \Delta F_{ziR} &= -\Delta F_{zi} \\
F_{ziL} &= \frac{1}{2} F_{zi} + \Delta F_{zi}, & F_{ziR} &= \frac{1}{2} F_{zi} - \Delta F_{zi}
\end{aligned} \tag{1.11}$$

The wheels at the front axle are steered about the king-pins with the angle δ. This angle relates directly to the imposed steering wheel angle δ_{stw} through the steering ratio n_{st}:

$$\delta = \frac{\delta_{\text{stw}}}{n_{\text{st}}} \tag{1.12}$$

In addition to this imposed steer angle, the wheels may show a steer angle and a camber angle induced by body roll through suspension kinematics. The functional relationships with the roll angle may be linearized. For axle i, we define

$$\begin{aligned}
\psi_{ri} &= \varepsilon_i \varphi \\
\gamma_{ri} &= \tau_i \varphi
\end{aligned} \tag{1.13}$$

Steer compliance gives rise to an additional steer angle due to the external torque that acts about the king-pin (steering axis). For the pair of front wheels, this torque results from the side force (and, of course, also from here not considered driving or braking forces) that exerts a moment about the king-pin through the moment arm which is composed of the caster length e and the pneumatic trail t_1. With the total steering stiffness $c_{\psi 1}$ felt about the king-pins with the steering wheel held fixed, the additional steer angle becomes when for simplicity the influence of camber on the pneumatic trail is disregarded:

$$\psi_{c1} = -\frac{F_{y1}(e + t_1)}{c_{\psi 1}} \tag{1.14}$$

In addition, the side force (but also the fore-and-aft force) may induce a steer angle due to suspension compliance. The so-called side force steer reads

$$\psi_{sfi} = c_{sfi} F_{yi} \tag{1.15}$$

For the front axle, we should separate the influences of moment steer and side force steer. For this reason, side force steer at the front is defined to occur as a result of the side force acting in a point on the king-pin axis.

Besides the wheel angles indicated above, the wheels may have been given initial angles that already exist at straight ahead running. These are the toe angle ψ_o (positive pointing outward) and the initial camber angle γ_o (positive: leaning outward). For the left and right wheels, we have the initial angles:

$$\begin{aligned}
\psi_{iLo} &= -\psi_{io}, \quad \psi_{iRo} = \psi_{io} \\
\gamma_{iLo} &= -\gamma_{io}, \quad \gamma_{iRo} = \gamma_{io}
\end{aligned} \tag{1.16}$$

Adding all relevant contributions (1.12) to (1.16) together yields the total steer angle for each of the wheels.

The effective cornering stiffness of an axle $C_{\text{eff},i}$ is now defined as the ratio of the axle side force and the virtual slip angle. This angle is defined as the angle between the direction of motion of the center of the axle i (actually at road level) when the vehicle velocity would be very low and approaches zero (then also $F_{yi} \to 0$) and the direction of motion at the actual speed considered. The virtual slip angle of the front axle has been indicated in Figure 1.4 and is designated as α_{a1}. We have, in general,

$$C_{\text{eff},i} = \frac{F_{yi}}{\alpha_{ai}} \tag{1.17}$$

The axle side forces in the steady-state turn can be derived by considering the lateral force and moment equilibrium of the vehicle:

$$F_{yi} = \frac{l - a_i}{l} m a_y \tag{1.18}$$

The axle side force is the sum of the left and right individual tire side forces. We have

$$F_{yiL} = \left(\tfrac{1}{2}C_{F\alpha i} + \zeta_{\alpha i}\Delta F_{zi}\right)(\alpha_i - \psi_{io}) + \left(\tfrac{1}{2}C_{F\gamma i} + \zeta_{\gamma i}\Delta F_{zi}\right)(\gamma_i - \gamma_{io})$$

$$F_{yiR} = \left(\tfrac{1}{2}C_{F\alpha i} - \zeta_{\alpha i}\Delta F_{zi}\right)(\alpha_i + \psi_{io}) + \left(\tfrac{1}{2}C_{F\gamma i} - \zeta_{\gamma i}\Delta F_{zi}\right)(\gamma_i + \gamma_{io}) \tag{1.19}$$

where the average wheel slip angle α_i indicated in the figure is

$$\alpha_i = \alpha_{ai} + \psi_i \tag{1.20}$$

and the average additional steer angle and the average camber angle are

$$\begin{aligned}
\psi_i &= \psi_{ri} + \psi_{ci} + \psi_{sfi} \\
\gamma_i &= \gamma_{ri}
\end{aligned} \tag{1.21}$$

The unknown quantity is the virtual slip angle α_{ai} which can be determined for a given lateral acceleration a_y. Next, we use Eqns (1.8, 1.9, 1.13, 1.18, 1.14, 1.15), substitute the resulting expressions (1.21) and (1.20) in (1.19), and add

up the two equations (1.19). The result is a relationship between the axle slip angle α_{ai} and the axle side force F_{yi}. We obtain, for the slip angle of axle i,

$$
\begin{aligned}
\alpha_{ai} &= \frac{F_{yi}}{C_{\text{eff},i}} \\
&= \frac{F_{yi}}{C_{F\alpha i}} \left[
\begin{array}{l}
1 + \dfrac{l(\varepsilon_i C_{F\alpha i} + \tau_i C_{F\gamma i})h'}{(l - a_i)(c_{\varphi 1} + c_{\varphi 2} - mgh')} + \dfrac{C_{F\alpha i}(e_i + t_i)}{c_{\psi i}} \\[2ex]
- C_{F\alpha i} c_{sfi} + \dfrac{2l\sigma_i}{l - a_i}(\zeta_{\alpha i}\psi_{io} + \zeta_{\gamma i}\gamma_{io})
\end{array}
\right]
\end{aligned}
\qquad (1.22)
$$

The coefficient of F_{yi} constitutes the effective axle cornering compliance, which is the inverse of the effective axle cornering stiffness (1.17). The quantitative effect of each of the suspension, steering, and tire factors included can be easily assessed. The subscript i refers to the complete axle. Consequently, the cornering and camber stiffnesses appearing in this expression are the sum of the stiffnesses of the left and right tire:

$$
\begin{aligned}
C_{F\alpha i} &= C_{F\alpha iL} + C_{F\alpha iR} = C_{F\alpha iLo} + C_{F\alpha iRo} \\
C_{F\gamma i} &= C_{F\gamma iL} + C_{F\gamma iR} = C_{F\gamma iLo} + C_{F\gamma iRo}
\end{aligned}
\qquad (1.23)
$$

in which (1.7) and (1.11) have been taken into account. The load transfer coefficient σ_i follows from Eqn (1.10). Expression (1.22) shows that the influence of lateral load transfer only occurs if initially, at straight ahead running, side forces are already present through the introduction of e.g., opposite steer and camber angles. If these angles are absent, the influence of load transfer is purely nonlinear and is only felt at higher levels of lateral accelerations. In the next subsection, this nonlinear effect will be incorporated in the effective axle characteristic.

Effective Nonlinear Axle Characteristics

To illustrate the method of effective axle characteristics, we will first discuss the determination of the effective characteristic of a front axle showing steering compliance. The steering wheel is held fixed. Due to tire side forces and self-aligning torques (left and right), distortions will arise resulting in an incremental steer angle ψ_{c1} of the front wheels (ψ_{c1} will be negative in Figure 1.5 for the case of just steer compliance). Since load transfer is not considered in this example, the situation at the left and right wheels is identical (initial toe and camber angles being disregarded). The front tire slip angle is denoted by α_1 and the 'virtual' slip angle of the axle is denoted by α_{a1} and equals (cf. Figure 1.5):

$$
\alpha_{a1} = \alpha_1 - \psi_{c1}
\qquad (1.24)
$$

where both α_1 and ψ_{c1} are related to F_{y1} and M_{z1}. The subscript 1 refers to the front axle and thus to the pair of tires. Consequently, F_{y1} and M_{z1} denote the sum of the left and right tire side forces and moments. The objective is to find the function $F_{y1}(\alpha_{a1})$ which is the effective front axle characteristic.
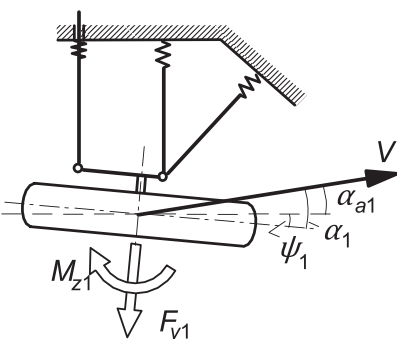
FIGURE 1.5 Wheel suspension and steering compliance resulting in additional steer angle ψ_1.

Figure 1.6 shows a graphical approach. According to Eqn (1.24), the points on the $F_{y1}(\alpha_1)$ curve must be shifted horizontally over a length ψ_{c1} to obtain the sought $F_{y1}(\alpha_{a1})$. The slope of the curve at the origin corresponds to the effective axle cornering stiffness found in the preceding subsection. Although the changes with respect to the original characteristic may be small, they can still be of considerable importance since it is the difference of slip angles front and rear which largely determines the vehicle's handling behavior.

The effective axle characteristic for the case of roll steer can be easily established by subtracting ψ_{ri} from α_i. Instead of using the linear relationships (1.8) and (1.13), nonlinear curves may be adopted, possibly obtained from measurements. For the case of roll camber, the situation becomes more complex. At a given axle side force, the roll angle and the associated camber
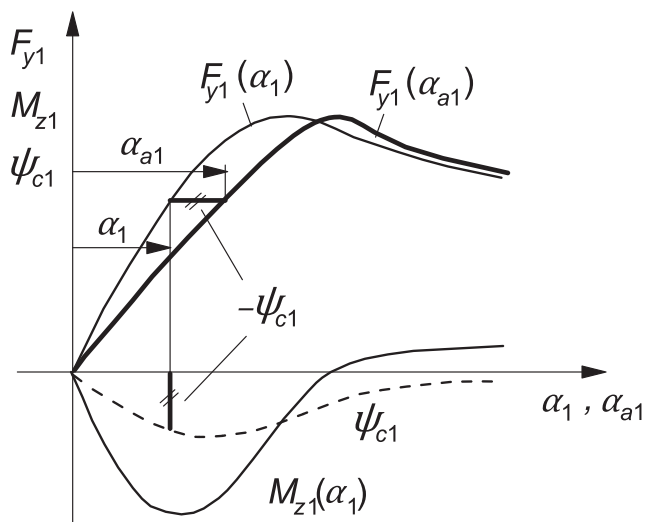

FIGURE 1.6 Effective front axle characteristic $F_{y1}(\alpha_{a1})$ influenced by steering compliance.
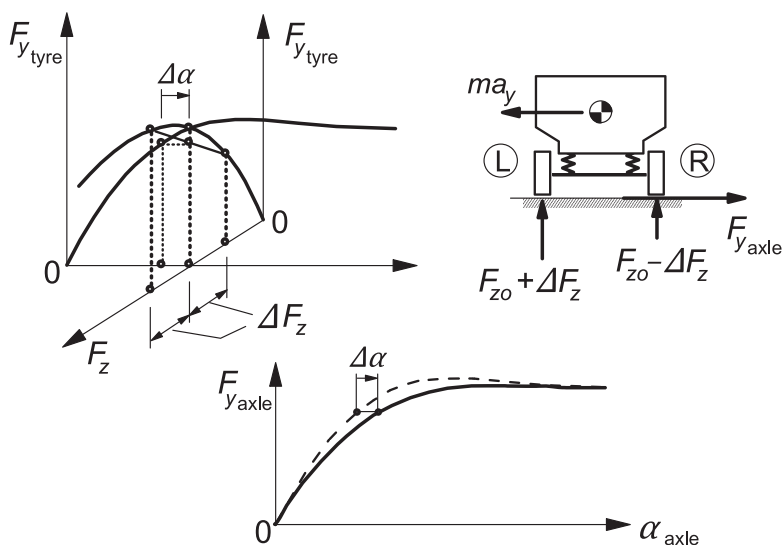
FIGURE 1.7 The influence of load transfer on the resulting axle characteristic.

angle can be found. The cornering characteristic of the pair of tires at that camber angle is needed to find the slip angle belonging to the side force considered.

Load transfer is another example that is less easy to handle. In Figure 1.7 a three-dimensional graph is presented for the variation of the side force of an individual tire as a function of the slip angle and of the vertical load, the former at a given load and the latter at a given slip angle. The diagram illustrates that at load transfer, the outer tire exhibiting a larger load will generate a larger side force than the inner tire. Because of the nonlinear degressive F_y vs F_z curve, however, the average side force will be smaller than the original value it had in the absence of load transfer. The graph indicates that an increased $\Delta\alpha$ of the slip angle would be needed to compensate for the adverse effect of load transfer. The lower diagram gives a typical example of the change in characteristic as a result of load transfer. At the origin the slope is not affected, but at larger slip angles an increasingly lower derivative appears to occur. The peak diminishes and may even disappear completely. The way to determine the resulting characteristic is the subject of the next exercise.

Exercise 1.1 Construction of Effective Axle Characteristics at Load Transfer

For a series of tire vertical loads, F_z, the characteristics of the two tires mounted on, say, the front axle of an automobile are given. In addition, it is known how the load transfer ΔF_z at the front axle depends on the centrifugal force $K (= mg\, F_{y1}/F_{z1} = mg\, F_{y2}/F_{z2})$ acting at the center of gravity. From these data, the resulting cornering characteristic of the axle considered (at steady-state cornering) can be determined.
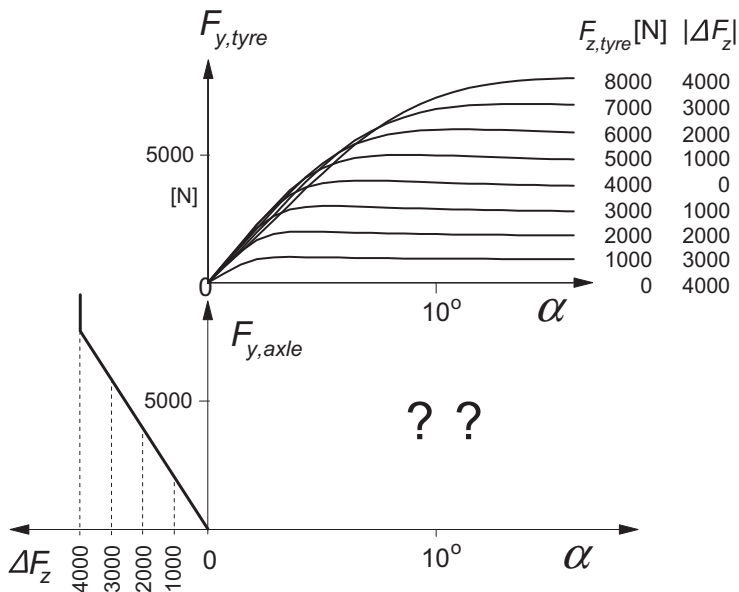
The figure shows an upper diagram with vertical axis $F_{y,tyre}$ and horizontal axis α (marked at $10°$), with a family of curves. To the right a table with columns $F_{z,tyre}$ [N] and $|\Delta F_z|$:

$F_{z,tyre}$ [N]	$|\Delta F_z|$
8000	4000
7000	3000
6000	2000
5000	1000
4000	0
3000	1000
2000	2000
1000	3000
0	4000

Lower diagram with vertical axis $F_{y,axle}$ and horizontal axis α (marked at $10°$), with "? ?" in the center. Left-hand diagram shows ΔF_z axis with values 4000, 3000, 2000, 1000, 0. Values 5000 marked on both upper and lower vertical axes, with [N].

FIGURE 1.8 The construction of the resulting axle cornering characteristics at load transfer (Exercise 1.1).

1. Find the resulting characteristic of one axle from the set of individual tire characteristics at different tire loads F_z and the load transfer characteristic, both shown in Figure 1.8.

   Hint: First draw, in the lower diagram, the axle characteristics for values of $\Delta F_z = 1000, 2000, 3000,$ and 4000 N and then determine which point on each of these curves is valid considering the load transfer characteristic (left-hand diagram). Draw the resulting axle characteristic.

   It may be helpful to employ the *Magic Formula* (1.6) and the parameters shown below:

   side force: $F_y = D \sin[C \arctan\{B\alpha - E(B\alpha - \arctan(B\alpha))\}]$
   with factors: $B = C_{F\alpha}/(CD)$, $C = 1.3$, $D = \mu F_z$, $E = -3$, with $\mu = 1$
   cornering stiffness: $C_{F\alpha} = c_1 \sin[2 \arctan\{F_z/c_2\}]$
   with parameters: $c_1 = 60000$ [N/rad], $c_2 = 4000$ [N]

   In addition, we have given, for the load transfer, $\Delta F_z = 0.52 F_{y,axle}$ (up to lift-off of the inner tire, after which the other axle may take over to accommodate the increased total load transfer).

2. Draw the individual curves of F_{yL} and F_{yR} (for the left and right tire) as a function of α which appear to arise under the load transfer condition considered here.

3. Finally, plot these forces as a function of the vertical load F_z (ranging from 0 to 8000 N). Note the variation of the lateral force of an individual (left or right) tire in this same range of vertical load which may be covered in a left- and in a right-hand turn at an increasing speed of travel until (and possibly beyond) the moment that one of the wheels (the inner wheel) lifts from the ground.

1.3. VEHICLE HANDLING AND STABILITY

In this section, attention is paid to the more fundamental aspects of vehicle horizontal motions. Instead of discussing results of computer simulations of complicated vehicle models, we rather take the simplest possible model of an automobile that runs at constant speed over an even horizontal road and thereby gain considerable insight into the basic aspects of vehicle handling and stability. Important early work on the linear theory of vehicle handling and stability has been published by Riekert and Schunck (1940), Whitcomb and Milliken (1956), and Segel (1956). Pevsner (1947) studied the nonlinear steady-state cornering behavior at larger lateral accelerations and introduced the handling diagram. One of the first more complete vehicle model studies has been conducted by Pacejka (1958) and by Radt and Pacejka (1963).

For more introductory or specialized study, the reader may be referred to books on the subject, cf. e.g.: Gillespie (1992), Mitschke (1990), Milliken and Milliken (1995), Kortüm and Lugner (1994), and Abe (2009).

The derivation of the equations of motion for the three degree of freedom model of Figure 1.4 will be treated first after which the simple model with two degrees of freedom is considered and analyzed. This analysis comprises the steady-state response to steering input and the stability of the resulting motion. Also, the frequency response to steering fluctuations and external disturbances will be discussed, first for the linear vehicle model and subsequently for the nonlinear model where large lateral accelerations and disturbances are introduced.

The simple model to be employed in the analysis is presented in Figure 1.9. The track width has been neglected with respect to the radius of the cornering motion which allows the use of a two-wheel vehicle model. The steer and slip angles will be restricted to relatively small values. Then, the variation of the geometry may be regarded to remain linear, that is, $\cos \alpha \approx 1$ and $\sin \alpha \approx \alpha$ and similarly for the steer angle δ. Moreover, the driving force required to keep the speed constant is assumed to remain small with respect to the lateral tire force.

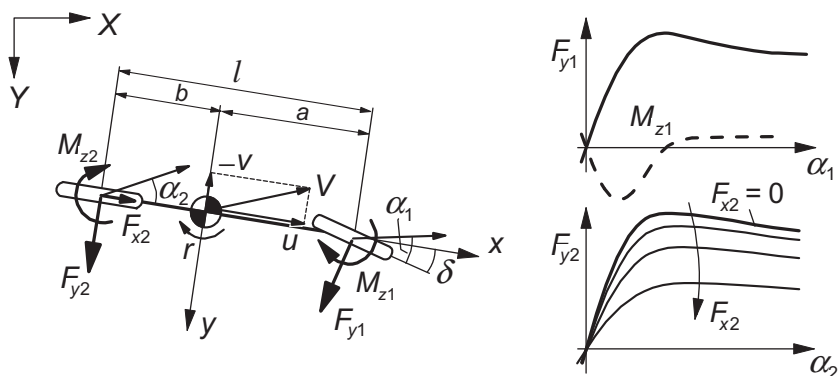

FIGURE 1.9   Simple car model with side force characteristics for front and rear (driven) axle.

Considering combined slip curves like those shown in Figure 1.2 (right), we may draw the conclusion that the influence of F_x on F_y may be neglected in that case.

In principle, a model as shown in Figure 1.9 lacks body roll and load transfer. Therefore, the theory is actually limited to cases where the roll moment remains small, that is, at low friction between tire and road or a low center of gravity relative to the track width. This restriction may be overcome by using the effective axle characteristics in which the effects of body roll and load transfer have been included while still adhering to the simple (rigid) two-wheel vehicle model. As mentioned before, this is only permissible when the frequency of the imposed steer angle variations remains small with respect to the roll natural frequency. Similarly, as demonstrated in the preceding section, effects of other factors like compliance in the steering system and suspension mounts may be accounted for.

The speed of travel is considered to be constant. However, the theory may approximately hold also for quasi-steady-state situations for instance at moderate braking or driving. The influence of the fore-and-aft force F_x on the tire or axle cornering force vs slip angle characteristic (F_y, α) may then be regarded (cf. Figure 1.9). The forces F_{y1} and F_{x1} and the moment M_{z1} are defined to act upon the single front wheel and similarly we define F_{y2} etc. for the rear wheel.

1.3.1. Differential Equations for Plane Vehicle Motions

In this section, the differential equations for the three degree of freedom vehicle model of Figure 1.4 will be derived. In first instance, the fore-and-aft motion will also be left free to vary. The resulting set of equations of motion may be of interest for the reader to further study the vehicle's dynamic response at somewhat higher frequencies where the roll dynamics of the vehicle body may become of importance, cf. App. 2. From these equations, the equations for the simple two-degree-of-freedom model of Figure 1.9 used in the subsequent section can be easily assessed. In Subsection 1.3.6, the equations for the car with trailer will be established. The possible instability of the motion will be studied.

We will employ Lagrange's equations to derive the equations of motion. For a system with n degrees of freedom n (generalized) coordinates, q_i are selected which are sufficient to completely describe the motion while possible kinematic constraints remain satisfied. The moving system possesses kinetic energy T and potential energy U. External generalized forces Q_i associated with the generalized coordinates q_i may act on the system. Internal forces acting from dampers to the system structure may be regarded as external forces taking part in the total work W. The equation of Lagrange for coordinate q_i reads

$$\frac{\mathrm{d}}{\mathrm{d}t}\frac{\partial T}{\partial \dot{q}_i} - \frac{\partial T}{\partial q_i} + \frac{\partial U}{\partial q_i} = Q_i \tag{1.25}$$

The system depicted in Figure 1.4 and described in the preceding subsection performs a motion over a flat level road. Proper coordinates are the Cartesian

coordinates X and Y of reference point A, the yaw angle ψ of the moving x-axis with respect to the inertial X-axis and finally the roll angle φ about the roll axis. For motions near the X-axis and thus small yaw angles, Eqn (1.25) is adequate to derive the equations of motion. For cases where ψ may attain large values, e.g., when moving along a circular path, it is preferred to use modified equations where the velocities u, v, and r of the moving axes system are used as generalized motion variables in addition to the coordinate φ. The relations between the two sets of variables are (the dots referring to differentiation with respect to time)

$$
\begin{aligned}
u &= \dot{X}\cos\psi + \dot{Y}\sin\psi \\
v &= -\dot{X}\sin\psi + \dot{Y}\cos\psi \\
r &= \dot{\psi}
\end{aligned}
\tag{1.26}
$$

The kinetic energy can be expressed in terms of u, v, and r. Preparation of the first terms of Eqn (1.25) for the coordinates X, Y, and ψ yields

$$
\begin{aligned}
\frac{\partial T}{\partial \dot{X}} &= \frac{\partial T}{\partial u}\frac{\partial u}{\partial \dot{X}} + \frac{\partial T}{\partial v}\frac{\partial v}{\partial \dot{X}} = \frac{\partial T}{\partial u}\cos\psi - \frac{\partial T}{\partial v}\sin\psi \\
\frac{\partial T}{\partial \dot{Y}} &= \frac{\partial T}{\partial u}\frac{\partial u}{\partial \dot{Y}} + \frac{\partial T}{\partial v}\frac{\partial v}{\partial \dot{Y}} = \frac{\partial T}{\partial u}\sin\psi + \frac{\partial T}{\partial v}\cos\psi \\
\frac{\partial T}{\partial \dot{\psi}} &= \frac{\partial T}{\partial r} \\
\frac{\partial T}{\partial \psi} &= \frac{\partial T}{\partial u}v - \frac{\partial T}{\partial v}u
\end{aligned}
\tag{1.27}
$$

The yaw angle ψ may now be eliminated by multiplying the final equations for X and Y successively with $\cos\psi$ and $\sin\psi$ and subsequently adding and subtracting them. The resulting equations represent the equilibrium in the x- and y- (or u and v) direction, respectively.

We obtain the following set of modified Lagrangian equations for the first three variables u, v, and r and subsequently for the remaining real coordinates (for our system only φ):

$$
\begin{aligned}
\frac{\mathrm{d}}{\mathrm{d}t}\frac{\partial T}{\partial u} - r\frac{\partial T}{\partial v} &= Q_u \\
\frac{\mathrm{d}}{\mathrm{d}t}\frac{\partial T}{\partial v} + r\frac{\partial T}{\partial u} &= Q_v \\
\frac{\mathrm{d}}{\mathrm{d}t}\frac{\partial T}{\partial r} - v\frac{\partial T}{\partial u} + u\frac{\partial T}{\partial v} &= Q_r \\
\frac{\mathrm{d}}{\mathrm{d}t}\frac{\partial T}{\partial \dot{\varphi}} - \frac{\partial T}{\partial \varphi} + \frac{\partial U}{\partial \varphi} &= Q_\varphi
\end{aligned}
\tag{1.28}
$$

The generalized forces are found from the virtual work:

$$\delta W = \sum_{j-1}^{4} Q_j \delta q_i \tag{1.29}$$

with q_j referring to the quasi-coordinates x and y and the coordinates ψ and φ. Note that x and y cannot be found from integrating u and v. For that reason, the term 'quasi' coordinate is used. For the vehicle model, we find for the virtual work as a result of the virtual displacements δx, δy, $\delta \psi$, and $\delta \varphi$:

$$\delta W = \sum F_x \delta x + \sum F_y \delta y + \sum M_z \delta \psi + \sum M_\varphi \delta \varphi \tag{1.30}$$

where apparently

$$
\begin{aligned}
Q_u &= \sum F_x = F_{x1} \cos \delta - F_{y1} \sin \delta + F_{x2} \\
Q_v &= \sum F_y = F_{x1} \sin \delta + F_{y1} \cos \delta + F_{y2} \\
Q_r &= \sum M_z = aF_{x1} \sin \delta + aF_{y1} \cos \delta + M_{z1} - bF_{y2} + M_{z2} \\
Q_\varphi &= \sum M_\varphi = -(k_{\varphi 1} + k_{\varphi 2})\dot{\varphi}
\end{aligned}
\tag{1.31}
$$

The longitudinal forces are assumed to be the same at the left and right wheels, and the effect of additional steer angles ψ_i is neglected here. Shock absorbers in the wheel suspensions are represented by the resulting linear moments about the roll axes with damping coefficients $k_{\varphi i}$ at the front and rear axles.

With the roll angle φ and the roll axis inclination angle $\theta_r \approx (h_2 - h_1)/l$ assumed small, the kinetic energy becomes

$$
\begin{aligned}
T = {}& \frac{1}{2}m\{(u - h'\varphi r)^2 + (v + h'\dot{\varphi})^2\} + \frac{1}{2}I_x \dot{\varphi}^2 \\
& + \frac{1}{2}I_y(\varphi r)^2 + \frac{1}{2}I_z(r^2 - \varphi^2 r^2 + 2\theta_r r\dot{\varphi}) - I_{xz}r\dot{\varphi}
\end{aligned}
\tag{1.32}
$$

The potential energy U is built up in the suspension springs (including the radial tire compliances) and through the height of the center of gravity. We have, again for small angles,

$$U = \frac{1}{2}(c_{\varphi 1} + c_{\varphi 2})\, \varphi^2 - \frac{1}{2}mgh'\varphi^2 \tag{1.33}$$

The equations of motion are finally established by using expressions (1.31), (1.32), and (1.33) in the Eqn (1.28). The equations will be linearized in the

supposedly small angles φ and δ. For the variables u, v, r, and φ, we obtain successively

$$m(\dot{u} - rv - h'\varphi\dot{r} - 2h'r\dot{\varphi}) = F_{x1} - F_{y1}\delta + F_{x2} \tag{1.34a}$$

$$m(\dot{v} + ru + h'\ddot{\varphi} - h'r^2\varphi) = F_{x1}\delta + F_{y1} + F_{y2} \tag{1.34b}$$

$$I_z\dot{r} + (I_z\theta_r - I_{xz})\ddot{\varphi} - mh'(\dot{u} - rv)\varphi = aF_{x1}\delta + aF_{y1} + M_{z1}$$

$$- bF_{y1} + M_{z1} - bF_{y2} + M_{z2} \tag{1.34c}$$

$$(I_X + mh'^2)\ddot{\varphi} + mh'(\dot{v} + ru) + (I_z\theta_r - I_{xz})\dot{r}$$

$$-(mh'^2 + I_y - I_z)r^2\varphi + (k_{\varphi1} + k_{\varphi2})\dot{\varphi}$$

$$+ (c_{\varphi1} + c_{\varphi2} - mgh')\varphi = 0 \tag{1.34d}$$

Note that the small additional roll and compliance steer angles ψ_i have been neglected in the assessment of the force components. The tire side forces depend on the slip and camber angles front and rear and on the tire vertical loads. We may need to take the effect of combined slip into account. The longitudinal forces are either given as a result of brake effort or imposed propulsion torque or they depend on the wheel longitudinal slip which follows from the wheel speed of revolution requiring four additional wheel rotational degrees of freedom. The first Eqn (1.34a) may be used to compute the propulsion force needed to keep the forward speed constant.

The vertical loads and more specifically the load transfer can be obtained by considering the moment equilibrium of the front and rear axle about the respective roll centers. For this, the roll moments $M_{\varphi i}$ (cf. Figure 1.4) resulting from suspension springs and dampers as appeared in Eqn (1.34d) through the terms with subscript 1 and 2 respectively, and the axle side forces appearing in Eqn (1.34b) are to be regarded. For a linear model the load transfer can be neglected if initial (left/right opposite) wheel angles are disregarded. We have at steady state (effect of damping vanishes)

$$\Delta F_{zi} = \frac{-c_{\varphi1}\varphi + F_{yi}h_i}{2s_i} \tag{1.35}$$

The front and rear slip angles follow from the lateral velocities of the wheel axles and the wheel steer angles with respect to the moving longitudinal x-axis. The longitudinal velocities of the wheel axles may be regarded the same left and right and equal to the vehicle longitudinal speed u. This is allowed when $s_i|r| \ll u$. Then the expressions for the assumedly small slip angles read

$$\alpha_1 = \delta + \psi_1 - \frac{v + ar - e\dot{\delta}}{u}$$

$$\alpha_2 = \psi_2 - \frac{v - br}{u} \tag{1.36}$$

The additional roll and compliance steer angles ψ_i and the wheel camber angles γ_i are obtained from Eqn (1.21) with (1.13–15) or corresponding nonlinear expressions. Initial wheel angles are assumed to be equal to zero. The influence of the steer angle velocity appearing in the expression for the front slip angle is relatively small and may be disregarded. The small products of the caster length e and the time rate of change of ψ_i have been neglected in the above expressions.

Equations (1.34) may be further linearized by assuming that all the deviations from the rectilinear motion are small. This allows neglecting all products of variable quantities which vanish when the vehicle moves straight ahead. The side forces and moments are then written as in Eqn (1.5) with the subscripts $i = 1$ or 2 provided. If the moment due to camber is neglected and the pneumatic trail is introduced in the aligning torque, we have

$$
\begin{aligned}
F_{y1} &= F_{y\alpha i} + F_{y\gamma i} = C_{F\alpha i}\alpha_i + C_{F\gamma i}\gamma_i \\
M_{zi} &= M_{z\alpha i} = -C_{M\alpha i}\alpha_i = -t_i F_{y\alpha i} = -t_i C_{F\alpha i}\alpha_i
\end{aligned}
\tag{1.37}
$$

The three linear equations of motion for the system of Figure 1.4 with the forward speed u kept constant finally turn out to read, if expressed solely in terms of the three motion variables v, r, and φ:

$$
\begin{aligned}
m(\dot{v} + ur + h'\ddot{\varphi}) &= C_{F\alpha 1}\{(1 + c_{sc1})(u\delta + e\dot{\delta} - v - ar)/u + c_{sr1}\varphi\} \\
&\quad + C_{F\alpha 2}\{(1 + c_{sc2})(-v + br)/u + c_{sr2}\varphi\} + (C_{F\gamma 1}\tau_1 + C_{F\gamma 2}\tau_2)\varphi
\end{aligned}
\tag{1.38a}
$$

$$
\begin{aligned}
I_z\dot{r} + (I_z\theta_r - I_{xz})\ddot{\varphi} &= (a - t_1)C_{F\alpha 1}\{(1 + c_{sc1})(u\delta + e\dot{\delta} - v - ar)/u + c_{sr1}\varphi\} \\
&\quad - (b + t_2)C_{F\alpha 2}\{(1 + c_{sc2})(-v + br)/u + c_{sr2}\varphi\} + (aC_{F\gamma 1}\tau_1 - bC_{F\gamma 2}\tau_2)\varphi
\end{aligned}
\tag{1.38b}
$$

$$
\begin{aligned}
&(I_x + mh'^2)\ddot{\varphi} + mh'(\dot{v} + ur) + (I_z\theta_r - I_{xz})\dot{r} \\
&+ (k_{\varphi 1} + k_{\varphi 2})\dot{\varphi} + (c_{\varphi 1} + c_{\varphi 2} - mgh')\varphi = 0
\end{aligned}
\tag{1.38c}
$$

In these equations, the additional steer angles ψ_i have been eliminated by using expressions (1.21) with (1.13–15). Furthermore, the resulting compliance steer and roll steer coefficients for $i = 1$ or 2 have been introduced:

$$
c_{sci} = \frac{A_i C_{F\alpha i}}{1 - A_i C_{F\alpha i}}, \quad c_{sri} = \frac{\varepsilon_i + \tau_i A_i C_{F\gamma i}}{1 - A_i C_{F\alpha i}}
\tag{1.39}
$$

with

$$
A_i = c_{sfi} - \frac{e_i + t_i}{c_{\psi i}}
$$

where the steer stiffness at the rear $c_{\psi 2}$ may be taken equal to infinity. Furthermore, we have the roll axis inclination angle:

$$\theta_r = \frac{h_2 - h_1}{l} \tag{1.40}$$

In Chapters 7 and 8, the transient properties of the tire will be addressed. The relaxation length denoted by σ_i is an important parameter that controls the lag of the response of the side force to the input slip angle. For the Laplace transformed version of Eqn (1.38) with the Laplace variable s representing differentiation with respect to time, we may introduce tire lag by replacing the slip angle α_i with the filtered transient slip angle. This may be accomplished by replacing the cornering stiffnesses $C_{F\alpha i}$ appearing in (1.38) and (1.39) with the 'transient stiffnesses':

$$C_{F\alpha i} \;\rightarrow\; \frac{C_{F\alpha i}}{1 + s\sigma_i/u} \tag{1.41}$$

A similar procedure may be followed to include the tire transient response to wheel camber variations. The relaxation length concerned is about equal to the one used for the response to side slip variations. At nominal vertical load, the relaxation length is of the order of magnitude of the wheel radius. A more precise model of the aligning torque may be introduced by using a transient pneumatic trail with a similar replacement as indicated by (1.41) but with a much smaller relaxation length approximately equal to half the contact length of the tire. For more details, we refer to Chapter 9 that is dedicated to short wavelength force and moment response.

1.3.2. Linear Analysis of the Two-Degree-of-Freedom Model

From Eqns (1.34b and c), the reduced set of equations for the two-degree-of-freedom model can be derived immediately. The roll angle φ and its derivative are set equal to zero and, furthermore, we will assume the forward speed u ($\approx V$) to remain constant and neglect the influence of the lateral component of the longitudinal forces F_{xi}. The equations of motion of the simple model of Figure 1.9 for v and r now read

$$m(\dot{v} + ur) = F_{y1} + F_{y2} \tag{1.42a}$$

$$I\dot{r} = aF_{y1} - bF_{y2} \tag{1.42b}$$

with v denoting the lateral velocity of the center of gravity and r the yaw velocity. The symbol m stands for the vehicle mass and I ($= I_z$) denotes the moment of inertia about the vertical axis through the center of gravity. For the matter of simplicity, the rearward shifts of the points of application of the forces F_{y1} and F_{y2} over a length equal to the pneumatic trail t_1 and t_2 respectively (that

is the aligning torques) have been disregarded. Later, we come back to this. The side forces are functions of the respective slip angles:

$$F_{y1} = F_{y1}(\alpha_1) \quad \text{and} \quad F_{y2} = F_{y2}(\alpha_2) \tag{1.43}$$

and the slip angles are expressed by

$$\alpha_1 = \delta - \frac{1}{u}(v + ar) \quad \text{and} \quad \alpha_2 = -\frac{1}{u}(v - br) \tag{1.44}$$

neglecting the effect of the time rate of change of the steer angle appearing in Eqn (1.36). For relatively low-frequency motions, the effective axle characteristics or effective cornering stiffnesses according to Eqns (1.17, 1.22) may be employed.

When only small deviations with respect to the undisturbed straight-ahead motion are considered, the slip angles may be assumed to remain small enough to allow linearization of the cornering characteristics. For the side force, the relationship with the slip angle reduces to the linear equation

$$F_{yi} = C_i \alpha_i = C_{F\alpha i} \alpha_i \tag{1.45}$$

where C_i denotes the cornering stiffness. This can be replaced by the symbol $C_{F\alpha i}$ which may be preferred in more general cases where also camber and aligning stiffnesses play a role.

The two linear first-order differential equations now read:

$$m\dot{v} + \frac{1}{u}(C_1 + C_2)v + \left\{ mu + \frac{1}{u}(aC_1 - bC_2) \right\} r = C_1\delta$$
$$I\dot{r} + \frac{1}{u}(a^2C_1 - b^2C_2)r + \frac{1}{u}(aC_1 - bC_2)v = aC_1\delta \tag{1.46}$$

After elimination of the lateral velocity v, we obtain the second-order differential equation for the yaw rate r:

$$Imu\ddot{r} + \{I(C_1 + C_2) + m(a^2C_1 + b^2C_2)\}\,\dot{r}$$
$$+ \frac{1}{u}\{C_1C_2l^2 - mu^2(aC_1 - bC_2)\}r = muaC_1\dot{\delta} + C_1C_2l\delta \tag{1.47}$$

Here, as before, the dots refer to differentiation with respect to time, δ is the steer angle of the front wheel, and $l\,(= a + b)$ represents the wheel base. The equations may be simplified by introducing the following quantities:

$$C = C_1 + C_2$$
$$Cs = aC_1 - bC_2$$
$$Cq^2 = a^2C_1 + b^2C_2$$
$$mk^2 = I \tag{1.48}$$

Here C denotes the total cornering stiffness of the vehicle, s is the distance from the center of gravity to the so-called neutral steer point S (Figure 1.11), q is

a length corresponding to an average moment arm, and k is the radius of gyration. Equations (1.46) and (1.47) now reduce to

$$m(\dot{v} + ur) + \frac{C}{u}v + \frac{Cs}{u}r = C_1\delta, \qquad mk^2\dot{r} + \frac{Cq^2}{u}r + \frac{Cs}{u}v = C_1a\delta \qquad (1.49)$$

and, with v eliminated,

$$m^2k^2u^2\ddot{r} + mC(q^2 + k^2)u\dot{r} + (C_1C_2l^2 - mu^2Cs)r = mu^2aC_1\dot{\delta} + uC_1C_2l\delta \tag{1.50}$$

The neutral steer point S is defined as the point on the longitudinal axis of the vehicle where an external side force can be applied without changing the vehicle's yaw angle. If the force acts in front of the neutral steer point, the vehicle is expected to yaw in the direction of the force and, if behind, then against the force. The point is of interest when discussing the steering characteristics and stability.

Linear Steady-State Cornering Solutions

We are interested in the path curvature $(1/R)$ that results from a constant steer angle δ at a given constant speed of travel V. Since we have at steady state

$$\frac{1}{R} = \frac{r}{V} \approx \frac{r}{u} \tag{1.51}$$

the expression for the path curvature becomes by using (1.47) with u replaced by V and the time derivatives omitted:

$$\frac{1}{R} = \frac{C_1C_2l}{C_1C_2l^2 - mV^2(aC_1 - bC_2)}\delta \tag{1.52}$$

By taking the inverse, the expression for the steer angle required to negotiate a curve with a given radius R is obtained:

$$\delta = \frac{1}{R}\left(l - mV^2\frac{aC_1 - bC_2}{lC_1C_2}\right) \tag{1.53}$$

It is convenient to introduce the so-called understeer coefficient or gradient η. For our model, this quantity is defined as

$$\eta = -\frac{mg}{l}\frac{aC_1 - bC_2}{C_1C_2} = -\frac{s}{l}\frac{mgC}{C_1C_2} \tag{1.54}$$

with g denoting the acceleration due to gravity. After having defined the lateral acceleration which in the present linear analysis equals the centripetal acceleration,

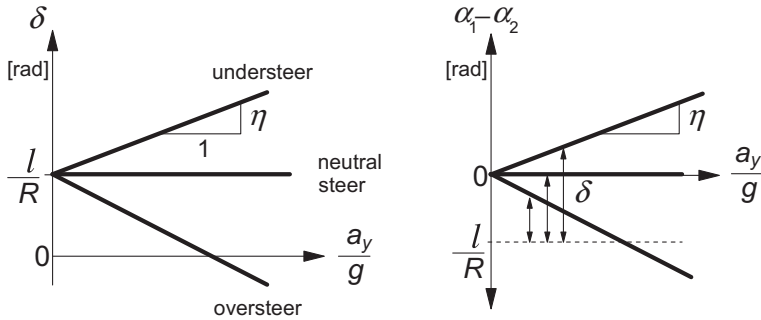$$a_y = Vr = \frac{V^2}{R} \tag{1.55}$$

FIGURE 1.10   The steer angle versus lateral acceleration at constant path curvature (left graph). The difference in slip angle versus lateral acceleration and the required steer angle at a given path curvature (right graph). The understeer gradient η.

Equation (1.53) can be written in the more convenient form:

$$\delta = \frac{l}{R}\left(1 + \eta\frac{V^2}{gl}\right) = \frac{l}{R} + \eta\frac{a_y}{g} \tag{1.56}$$

The meaning of understeer versus oversteer becomes clear when the steer angle is plotted against the centripetal acceleration while the radius R is kept constant. In Figure 1.10 (left-hand diagram) this is done for three types of vehicles showing understeer, neutral steer, and oversteer. Apparently, for an understeered vehicle, the steer angle needs to be increased when the vehicle is going to run at a higher speed. At neutral steer the steer angle can be kept constant, while at oversteer a reduction in steer angle is needed when the speed of travel is increased and at the same time a constant turning radius is maintained.

According to Eqn (1.56), the steer angle changes sign when, for an oversteered car, the speed increases beyond the critical speed that is expressed by

$$V_{crit} = \sqrt{\frac{gl}{-\eta}} \quad (\eta < 0) \tag{1.57}$$

As will be shown later, the motion becomes unstable when the critical speed is surpassed. Apparently, this can only happen when the vehicle shows oversteer.

For an understeered car, a counterpart has been defined which is the so-called characteristic speed. It is the speed where the steer angle required to maintain the same curvature increases twice the angle needed at speeds approaching zero. We may also say that at the characteristic speed the path curvature response to steer angle has decreased to half its value at very low speed. Also interesting is the fact that at the characteristic speed, the yaw rate

response to steer angle r/δ reaches a maximum (the proof of which is left to the reader). We have, for the characteristic velocity,

$$V_{\text{char}} = \sqrt{\frac{gl}{\eta}} \quad (\eta > 0) \tag{1.58}$$

Expression (1.54) for the understeer gradient η is simplified when the following expressions for the front and rear axle loads are used:

$$F_{z1} = \frac{b}{l}mg \quad \text{and} \quad F_{z2} = \frac{a}{l}mg \tag{1.59}$$

We obtain

$$\eta = \frac{F_{z1}}{C_1} - \frac{F_{z2}}{C_2} \tag{1.60}$$

which says that a vehicle exhibits an understeer nature when the relative cornering compliance of the tires at the front is larger than at the rear. It is important to note that in (1.59) and (1.60), the quantities $F_{z1,2}$ denote the vertical axle loads that occur at stand-still and thus represent the mass distribution of the vehicle. Changes of these loads due to aerodynamic down forces and fore-and-aft load transfer at braking or driving should not be introduced in expression (1.60).

In the same diagram, the difference in slip angle front and rear may be indicated. We find, for the side forces,

$$F_{y1} = \frac{b}{l}ma_y = F_{z1}\frac{a_y}{g}, \quad F_{y2} = \frac{a}{l}ma_y = F_{z2}\frac{a_y}{g} \tag{1.61}$$

and hence, for the slip angles,

$$\alpha_1 = \frac{F_{z1}}{C_1}\frac{a_y}{g}, \quad \alpha_2 = \frac{F_{z2}}{C_2}\frac{a_y}{g} \tag{1.62}$$

The difference now reads when considering relation (1.59):

$$\alpha_1 - \alpha_2 = \eta\frac{a_y}{g} \tag{1.63}$$

Apparently, the sign of this difference is dictated by the understeer coefficient. Consequently, it may be stated that according to the linear model, an understeered vehicle ($\eta > 0$) moves in a curve with slip angles larger at the front than at the rear ($\alpha_1 > \alpha_2$). For a neutrally steered vehicle, the angles remain the same ($\alpha_1 = \alpha_2$) and with an oversteered car the rear slip angles are bigger ($\alpha_2 > \alpha_1$). As shown by the expressions (1.54), the signs of η and s are different. Consequently, as one might expect when the centrifugal force is considered as the external force, a vehicle acts oversteered when the neutral steer point lies in front of the center of gravity and understeered when S lies behind the c.g. As we will see later on, the actual nonlinear vehicle may change its steering character

when the lateral acceleration increases. It appears then that the difference in slip angle is no longer directly related to the understeer gradient.

Considering Eqn (1.56) reveals that on the left-hand graph of Figure 1.10, the difference in slip angle can be measured along the ordinate starting from the value l/R. It is of interest to convert the diagram into the graph shown on the right-hand side of Figure 1.10 with ordinate equal to the difference in slip angle. In that way, the diagram becomes more flexible because the value of the curvature l/R may be selected afterward. The horizontal dotted line is then shifted vertically according to the value of the relative curvature l/R considered. The distance to the handling line represents the magnitude of the steer angle.

Figure 1.11 depicts the resulting steady-state cornering motion. The vehicle side slip angle β has been indicated. It is of interest to note that at low speed this angle is negative for right-hand turns. Beyond a certain value of speed, the tire slip angles have become sufficiently large and the vehicle slip angle changes into positive values. In Exercise 1.2 the slip angle β will be used.

Influence of the Pneumatic Trail

The direct influence of the pneumatic trails t_i may not be negligible. In reality, the tire side forces act a small distance behind the contact centers. As a consequence, the neutral steer point should also be considered to be located at a distance approximately equal to the average value of the pneumatic trails, more to the rear, which means actually more understeer. The correct
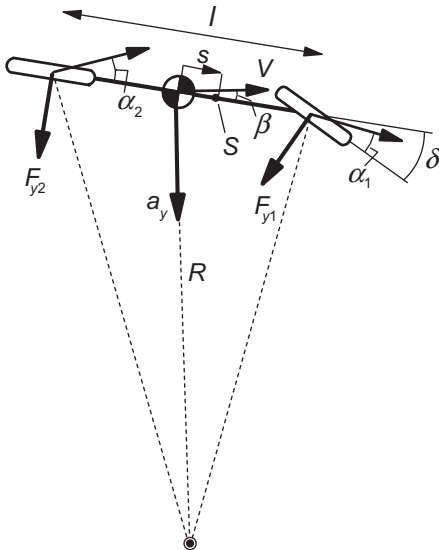

FIGURE 1.11 Two-wheel vehicle model in a cornering maneuver.

values of the position s of the neutral steer point and of the understeer coefficient η can be found by using the effective axle distances $a' = a - t_1$, $b' = b + t_2$, and $l' = a' + b'$ in Eqns (1.48) and (1.59) instead of the original quantities a, b, and l.

Stability of the Motion

Stability of the steady-state circular motion can be examined by considering the differential Eqn (1.47) or (1.50). The steer angle is kept constant so that the equation gets the form

$$a_0 \ddot{r} + a_1 \dot{r} + a_2 r = b_1 \delta \tag{1.64}$$

For this second-order differential equation, stability is assured when all coefficients a_i are positive. Only the last coefficient a_2 may become negative which corresponds to divergent instability (spin-out without oscillations). As already indicated, this will indeed occur when, for an oversteered vehicle, the critical speed (1.57) is exceeded. The condition for stability reads

$$a_2 = C_1 C_2 l^2 \left(1 + \eta \frac{V^2}{gl} \right) = C_1 C_2 l^2 \left(\frac{\delta}{l/R} \right)_{ss} > 0 \tag{1.65}$$

with the subscript ss referring to steady-state conditions, or

$$V < V_{\text{crit}} = \sqrt{\frac{gl}{-\eta}} \quad (\eta < 0) \tag{1.66}$$

The next section will further analyze the dynamic nature of the stable and unstable motions.

It is of importance to note that when the condition of an automobile subjected to driving or braking forces is considered, the cornering stiffnesses front and rear will change due to the associated fore-and-aft axle load transfer and the resulting state of combined slip. In expression (1.60) for the understeer coefficient η, the quantities F_{zi} represent the static vertical axle loads obtained through Eqn (1.59) and are to remain unchanged! In Subsection 1.3.4, the effect of longitudinal forces on vehicle stability will be further analyzed.

Free Linear Motions

To study the nature of the free motion after a small disturbance in terms of natural frequency and damping, the eigenvalues, that is the roots of the characteristic equation of the linear second-order system, are to be assessed.

The characteristic equation of the system described by the Eqn (1.49) or (1.50) reads after using the relation (1.54) between s and η:

$$m^2 k^2 V^2 \lambda^2 + mC(q^2 + k^2)V\lambda + C_1 C_2 l^2 \left(1 + \frac{\eta}{gl} V^2\right) = 0 \qquad (1.67)$$

For a single mass–damper–spring system shown in Figure 1.13 with r the mass displacement, δ the forced displacement of the support, M the mass, D the sum of the two damping coefficients D_1 and D_2, and K the sum of the two spring stiffnesses K_1 and K_2, a differential equation similar in structure to Eqn (1.50) arises:

$$M\ddot{r} + D\dot{r} + Kr = D_1\dot{\delta} + K_1\delta \qquad (1.68)$$

and the corresponding characteristic equation:

$$M\lambda^2 + D\lambda + K = 0 \qquad (1.69)$$

When an oversteered car exceeds its critical speed, the last term of (1.67) becomes negative which apparently corresponds to a negative stiffness K. An inverted pendulum is an example of a second-order system with negative last coefficient showing monotonous (diverging) instability.

The roots λ of Eqn (1.67) may have loci in the complex plane as shown in Figure 1.12. For positive values of the cornering stiffnesses, only the last coefficient of the characteristic equation can become negative which is responsible for the limited types of eigenvalues that can occur. As we will see in Subsection 1.3.3, possible negative slopes beyond the peak of the nonlinear axle characteristics may give rise to other types of unstable motions connected with two positive real roots or two conjugated complex
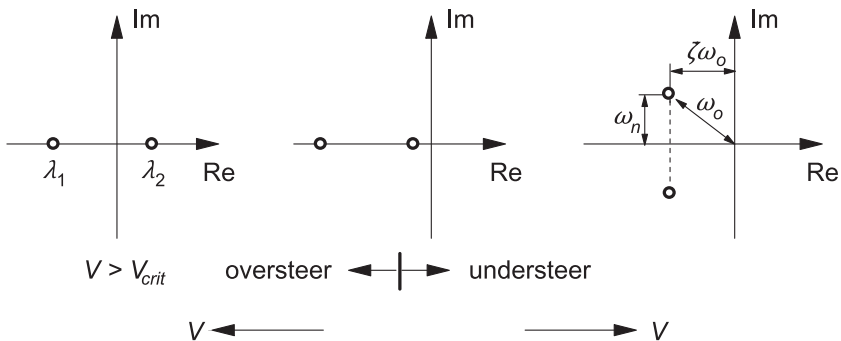

FIGURE 1.12 Possible eigenvalues for the over- and understeered car at lower and higher speeds.

roots with a positive real part. For the linear vehicle model, we may have two real roots in the oversteer case and a pair of complex roots in the understeer case, except at low speeds where the understeered vehicle can show a pair of real negative roots.

As indicated in the figure, the complex root is characterized by the natural frequency ω_o of the undamped system ($D = 0$), the damping ratio ζ, and the resulting actual natural frequency ω_n. Expressions for these quantities in terms of the model parameters are rather complex. However, if we take into account that in normal cases $|s| \ll l$ and $q \approx k \approx \frac{1}{2} l$, we may simplify these expressions and find the following useful formulas:

The natural frequency of the undamped system:

$$\omega_o^2 = \frac{K}{M} \approx \left(\frac{C}{mV}\right)^2 \cdot \left(1 + \frac{\eta}{gl}V^2\right) \tag{1.70}$$

The damping ratio:

$$\zeta = \frac{D}{2M\omega_o} \approx \frac{1}{\sqrt{1 + \dfrac{\eta}{gl}V^2}} \tag{1.71}$$

The natural frequency:

$$\omega_n^2 = \omega_o^2\left(1 - \zeta^2\right) \approx \left(\frac{C}{m}\right)^2 \cdot \frac{\eta}{gl} \tag{1.72}$$

The influence of parameters has been indicated in Figure 1.13. An arrow pointing upward represents an increase of the quantity in the same column of the matrix.
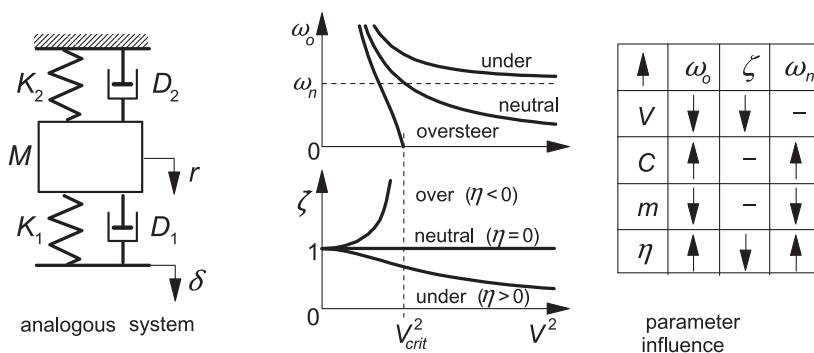

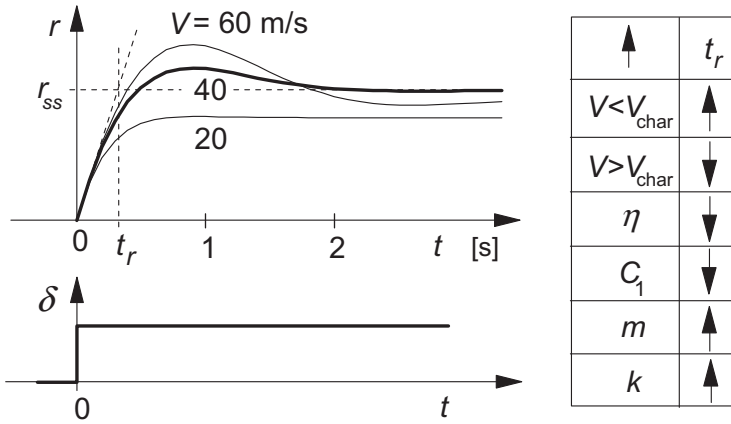**FIGURE 1.13**   The influence of parameters on natural frequency and damping.

FIGURE 1.14 Step response of yaw rate to steer angle. Parameters according to Table 1.1. Parameter influence on the rise time t_r.

The yaw rate response to a step change in steer angle is typified by the rise time t_r indicated in Figure 1.14 and expressed in terms of the parameters as follows:

$$t_r = \frac{r_{ss}}{\left(\frac{\partial r}{\partial t}\right)_{t=0}} = \frac{mk^2 V}{aC_1 l\left(1 + \frac{\eta}{gl}V^2\right)} = \frac{mk^2 V}{\frac{a}{l}\left\{C_1 l^2 + \left(b - a\frac{C_1}{C_2}\right)mV^2\right\}} \quad (1.73)$$

which may be readily obtained with the aid of Eqns (1.46, 1.47).

The parameter influence has been indicated in the figure. The results correspond qualitatively well with the 90% response times found in vehicle model simulation studies. A remarkable result is that for an understeered automobile, the response time is smaller than for an oversteered car.

Forced Linear Vibrations

The conversion of the equations of motion (1.46) into the standard state space representation is useful when the linear system properties are the subject of investigation. The system at hand is of the second order and hence possesses two state variables for which we choose v and r. The system is subjected to a single input signal: the steer angle δ. Various variables may be of interest to analyze the vehicle's response to steering input oscillations. The following quantities are selected to illustrate the method and to study the dynamic behavior of the vehicle: the lateral acceleration a_y of the center of gravity of the vehicle, the yaw rate r, and the vehicle slip angle β defined at the center of gravity. In matrix notation, the equation becomes

$$\dot{x} = Ax + Bu$$

$$y = Cx + Du \quad (1.74)$$

with

$$\dot{x} = \begin{pmatrix} \dot{v} \\ \dot{r} \end{pmatrix}, \quad u = \delta, \quad y = \begin{pmatrix} a_y \\ r \\ \beta \end{pmatrix} = \begin{pmatrix} \dot{v} + Vr \\ r \\ -v/V \end{pmatrix} \tag{1.75}$$

and

$$A = -\begin{pmatrix} \dfrac{C}{mV} & V + \dfrac{Cs}{mV} \\ \dfrac{Cs}{mk^2V} & \dfrac{Cq^2}{mk^2V} \end{pmatrix}, \quad B = \begin{pmatrix} \dfrac{C_1}{m} \\ \dfrac{C_1a}{mk^2} \end{pmatrix}$$

$$C = -\begin{pmatrix} \dfrac{C}{mV} & \dfrac{Cs}{mV} \\ 0 & -1 \\ 1/V & 0 \end{pmatrix}, \quad D = \begin{pmatrix} \dfrac{C_1}{m} \\ 0 \\ 0 \end{pmatrix}$$

The frequency response functions have been computed using Matlab software. Figure 1.15 presents the amplitude and phase response functions for each of the three output quantities and at three different values of speed of travel. The values of the chosen model parameters and a number of characteristic quantities have been listed in Table 1.1.

Explicit expressions of the frequency response functions in terms of model parameters are helpful to understand and predict the characteristic aspects of these functions which may be established by means of computations or possibly through full-scale experiments.

From the differential Eqn (1.50), the frequency response function is easily derived. Considering the quantities formulated by (1.70) and (1.71) and the steady-state response $(r/\delta)_{ss} = (V/R)/\delta$ obtained from (1.56), we find

$$\frac{r}{\delta}(j\omega) = \left(\frac{r}{\delta}\right)_{ss} \cdot \frac{1 + \dfrac{mVa}{C_2l}j\omega}{1 - \left(\dfrac{\omega}{\omega_o}\right)^2 + 2\zeta\left(\dfrac{j\omega}{\omega_o}\right)}; \quad \left(\frac{r}{\delta}\right)_{ss} = \frac{V/l}{1 + \dfrac{\eta}{gl}V^2} \tag{1.77}$$

Similarly, the formula for the response of lateral acceleration a_y can be derived:

$$\frac{a_y}{\delta}(j\omega) = \left(\frac{a_y}{\delta}\right)_{ss} \cdot \frac{1 - \dfrac{mk^2}{C_2l}\omega^2 + \dfrac{b}{V}j\omega}{1 - \left(\dfrac{\omega}{\omega_o}\right)^2 + 2\zeta\left(\dfrac{j\omega}{\omega_o}\right)}; \quad \left(\frac{a_y}{\delta}\right)_{ss} = \frac{V^2/l}{1 + \dfrac{\eta}{gl}V^2} \tag{1.78}$$
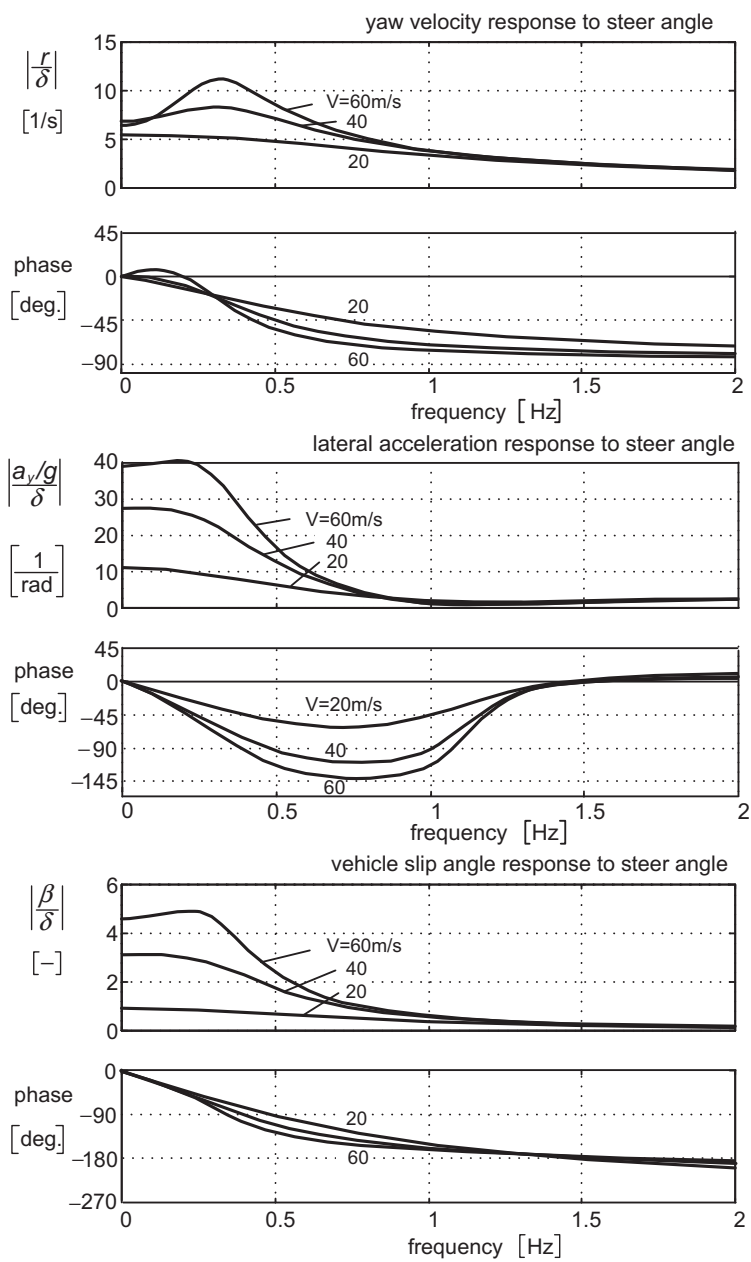
FIGURE 1.15 Frequency response functions; vehicle parameters according to Table 1.1.

TABLE 1.1 Parameter Values and Typifying Quantities

Parameters				Derived Typifying Quantities			
a	1.4 m	l	3 m	V [m/s]	20	40	60
b	1.6 m	F_{z1}	8371 N	ω_o [rad/s]	4.17	2.6	2.21
C_1	60000 N/rad	F_{z2}	7325 N	ζ [−]	0.9	0.7	0.57
C_2	60000 N/rad	q	1.503 m	ω_n [rad/s]	1.8	1.8	1.82
m	1600 kg	s	−0.1 m	t_r [s]	0.23	0.3	0.27
k	1.5 m	η	0.0174 rad (~1° extra steer/g lateral acceleration)				

And, for the slip angle β,

$$\frac{\beta}{\delta}(j\omega) = \left(\frac{\beta}{\delta}\right)_{ss} \cdot \frac{1 - \dfrac{mk^2V}{amV^2 - bC_2l}j\omega}{1 - \left(\dfrac{\omega}{\omega_o}\right)^2 + 2\zeta\left(\dfrac{j\omega}{\omega_o}\right)}; \quad \left(\frac{\beta}{\delta}\right)_{ss} = -\frac{b}{l}\frac{1 - \dfrac{a}{b}\dfrac{m}{C_2l}V^2}{1 + \dfrac{\eta}{gl}V^2} \quad (1.79)$$

By considering Eqn (1.77), it can now be explained that for instance at higher frequencies the system exhibits features of a first-order system: because of the $j\omega$ term in the numerator, the yaw rate amplitude response tends to decay at a 6 dB per octave rate (when plotted in log–log scale) and the phase lag approaches 90 degrees. The phase increase at low frequencies and higher speeds is due to the presence of the same jw term in the numerator. At speeds beyond approximately the characteristic speed, the corresponding (last) term in the denominator has less influence on the initial slope of the phase characteristic. The lateral acceleration response (1.78) shown in the center graph of Figure 1.15 gives a finite amplitude at frequencies tending to infinity because of the presence of ω^2 in the numerator. For the same reason, the phase lag goes back to zero at large frequencies. The side slip phase response tends to −270 degrees (at larger speeds) which is due to the negative coefficient of $j\omega$ in the numerator of (1.79). This is in contrast to that coefficient of the yaw rate response (1.77).

It is of interest to see that the steady-state slip angle response, indicated in (1.79), changes sign at a certain speed V. At low speeds where the tire slip angles are still very small, the vehicle slip angle obviously is negative for positive steer angle (considering positive directions as adopted in Figure 1.11). At larger velocities, the tire slip angles increase and, as a result, β changes to the positive direction.

Exercise 1.2. Four-Wheel Steer at the Condition that the Vehicle Slip Angle Vanishes

Consider the vehicle model of Figure 1.16. Both the front and the rear wheels can be steered. The objective is to make the vehicle move at a slip angle β remaining equal to zero. In practice, this may be done to improve handling qualities of the automobile (reduces to first-order system!) and to avoid excessive side slipping motions of the rear axle in lane change maneuvers. Adapt the equations of motion (1.46) and assess the required relationship between the steer angles δ_1 and δ_2. Do this in terms of the transfer function between δ_2 and δ_1 and the associated differential equation. Find the steady-state ratio $(\delta_2/\delta_1)_{ss}$ and plot this as a function of the speed V. Show also the frequency response function δ_2/δ_1 $(j\omega)$ for the amplitude and phase at a speed $V = 30$ m/s. Use the vehicle parameters supplied in Table 1.1.
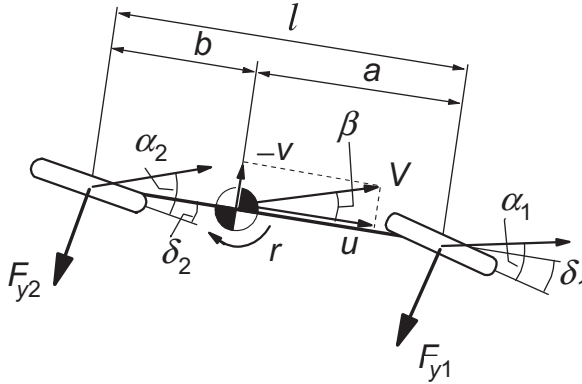

FIGURE 1.16 'Four-wheel' steering to make slip angle $\beta = 0$ (Exercise 1.2).

1.3.3. Nonlinear Steady-State Cornering Solutions

From Eqns (1.42) and (1.59) with the same restrictions as stated below Eqn (1.60), the following force balance equations can be derived (follows also from Eqn (1.61)). The effect of the pneumatic trails will be dealt with later on.

$$\frac{F_{y1}}{F_{z1}} = \frac{F_{y2}}{F_{z2}} = \frac{a_y}{g} \quad \left(= \frac{K}{mg} \right) \tag{1.80}$$

where $K = ma_y$ represents the centrifugal force. The kinematic relationship

$$\delta - (\alpha_1 - \alpha_2) = \frac{l}{R} \tag{1.81}$$

follows from Eqns (1.44) and (1.51). In Figure 1.11 the vehicle model has been depicted in a steady-state cornering maneuver. It can easily be observed from this diagram that relation (1.81) holds approximately when the angles are small.

The ratio of the side force and vertical load as shown in (1.80) plotted as a function of the slip angle may be termed as the normalized tire or axle characteristic. These characteristics subtracted horizontally from each other produce the 'handling curve'. Considering the equalities (1.80), the ordinate may be replaced by a_y/g. The resulting diagram with abscissa $\alpha_1 - \alpha_2$ is the nonlinear version of the right-hand diagram of Figure 1.10 (rotated 90° anti-clockwise). The diagram may be completed by attaching the graph that shows, for a series of speeds V, the relationship between lateral acceleration (in g units) a_y/g and the relative path curvature l/R according to Eqn (1.55).

Figure 1.17 shows the normalized axle characteristics and the completed handling diagram. The handling curve consists of a main branch and two side lobes. The different portions of the curves have been coded to indicate the corresponding parts of the original normalized axle characteristics they
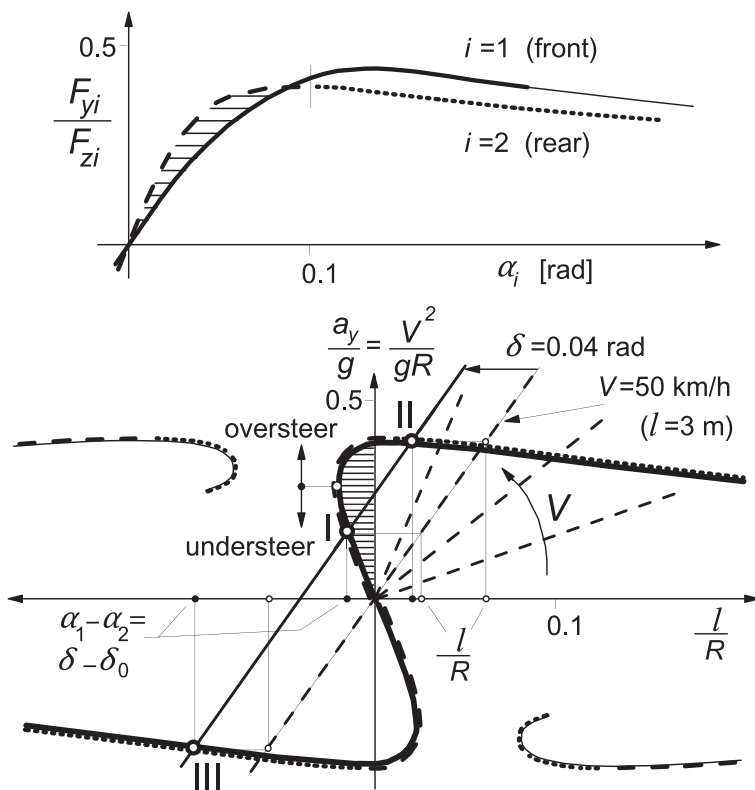

FIGURE 1.17 Handling diagram resulting from normalized tire characteristics. Equilibrium points I, II, and III (steady turns), of which only I is stable, arise for speed $V = 50$ km/h and steer angle $\delta = 0.04$ rad. From the different line types, the manner in which the curves are obtained from the upper diagram may be retrieved.

originate from. Near the origin, the system may be approximated by a linear model. Consequently, the slope of the handling curve in the origin with respect to the vertical axis is equal to the understeer coefficient η. In contrast to the straight handling line of the linear system (Figure 1.10), the nonlinear system shows a curved line. The slope changes along the curve which means that the degree of understeer changes with increasing lateral acceleration. The diagram of Figure 1.17 shows that the vehicle considered changes from understeer to oversteer. We define

$$\text{understeer if:} \quad \left(\frac{\partial \delta}{\partial V}\right)_R > 0$$

$$\text{oversteer if:} \quad \left(\frac{\partial \delta}{\partial V}\right)_R < 0 \qquad (1.82)$$

The family of straight lines represents the relationship between acceleration and curvature at different levels of speed. The speed line belonging to $V = 50$ km/h has been indicated (wheel base $l = 3$ m). This line is shifted to the left over a distance equal to the steer angle $\delta = 0.04$ rad and three points of intersection with the handling curve arise. These points I, II, and III indicate the possible equilibrium conditions at the chosen speed and steer angle. The connected values of the relative path curvature l/R can be found by going back to the speed line. As will be shown further on, only point I refers to a stable cornering motion. In points II and III ($R < 0$!), the motion is unstable.

At a given speed V, a certain steer angle δ is needed to negotiate a circular path with given radius R. The steer angle required can be read directly from the handling diagram. The steer angle needed to negotiate the same curve at very low speed ($V \to 0$) tends to l/R. This steer angle is denoted by δ_o. Consequently, the abscissa of the handling curve $\alpha_1 - \alpha_2$ may as well be replaced by $\delta - \delta_o$. This opens the possibility to determine the handling curve with the aid of simple experimental means, i.e., measuring the steering wheel input (reduced to equivalent road wheel steer angle by means of the steering ratio, which method automatically includes steering compliance effects) at various speeds running over the same circular path.

Subtracting normalized characteristics may give rise to very differently shaped handling curves only by slightly modifying the original characteristics. As Figure 1.17 shows, apart from the main branch passing through the origin, isolated branches may occur. These are associated with at least one of the decaying ends of the pair of normalized tire characteristics.

In Figure 1.18 a set of four possible combinations of axle characteristics have been depicted together with the resulting handling curves. This collection of characteristics shows that the nature of steering behavior is entirely governed by the normalized axle characteristics and in particular their relative shape with respect to each other.
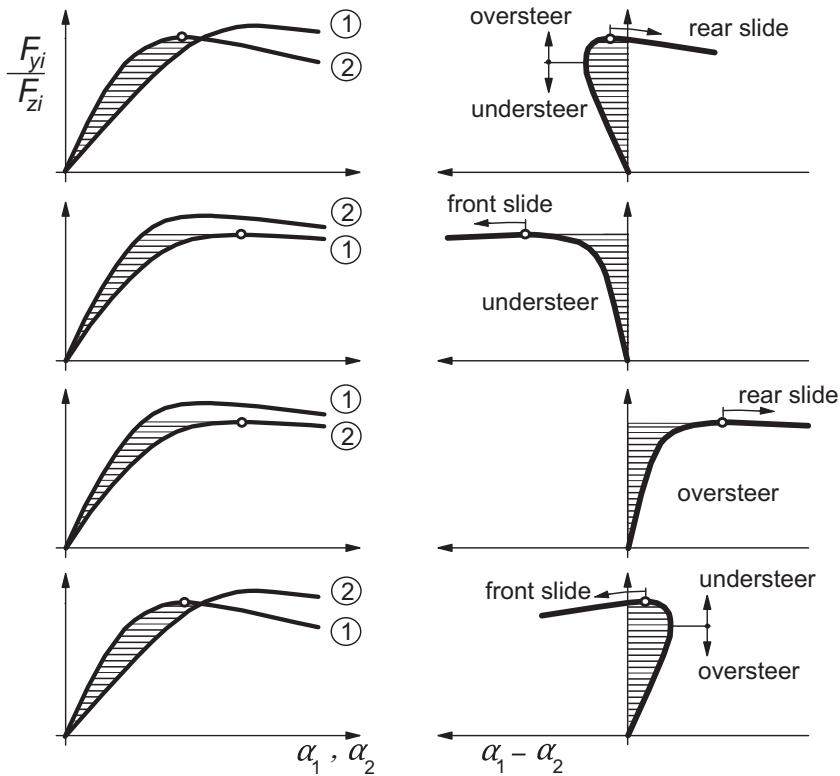
FIGURE 1.18 A number of handling curves arising from the pairs of normalized tire characteristics shown in left. Only the main branch of the handling curve has been drawn (1: front, 2: rear).

The way in which we can use the handling diagram is presented in Figure 1.19. The speed of travel may be kept constant and the lateral acceleration is increased by running over a spiral path with decreasing radius. The required variation of the steer angle follows from the distance between the handling curve and the speed line. Similarly, we can observe what happens when the path curvature is kept constant and the speed is increased. Also, the resulting variation of the curvature at a constant steer angle and increasing speed can be found. More general cases of quasi-steady-state motions may be studied as well.

Stability of the Motion at Large Lateral Accelerations

The nonlinear set of Eqns (1.42–44) may be linearized around the point of operation, which is one of the equilibrium states indicated above. The resulting second-order differential equation has a structure similar to Eqn (1.64) or (1.47)
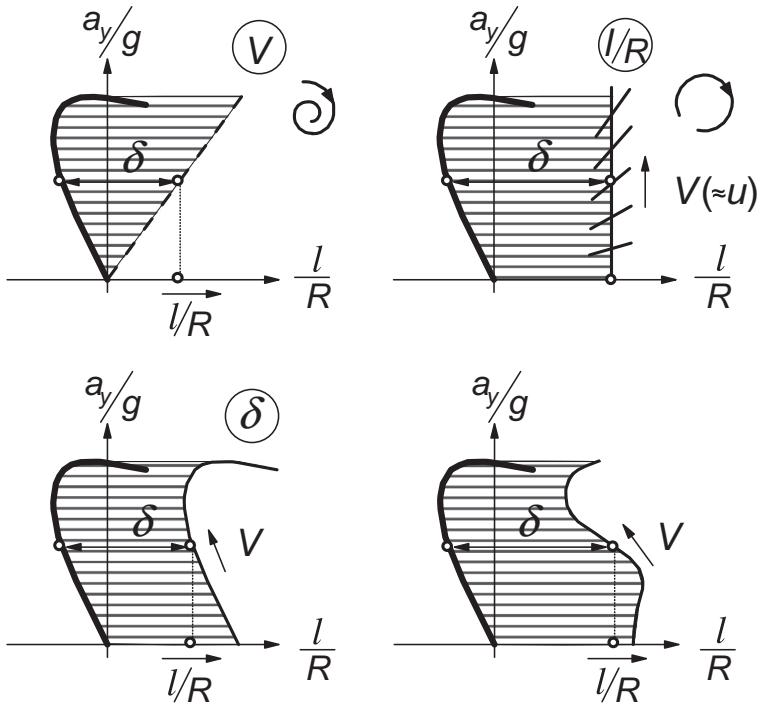
FIGURE 1.19 Types of quasi-steady-state maneuvers.

but with the variables replaced by their small variations with respect to the steady-state condition considered. Analysis of the coefficients of the characteristic equation reveals if stability exists. Also the nature of stability (monotonous, oscillatory) follows from these coefficients. This is reflected by the type of singular points (node, spiral, saddle) representing the equilibrium solutions in the phase plane as treated in the next section.

It now turns out that not only the last coefficient can become negative but also the second coefficient a_1. Instead of the cornering stiffnesses C defined in the origin of the tire cornering characteristics, the slope of the normalized characteristics at a given level of a_y/g becomes now of importance. We define

$$\Phi_i = \frac{1}{F_{zi}} \frac{\partial F_{yi}}{\partial \alpha_i} \quad (i = 1, 2) \tag{1.83}$$

The conditions for stability, that is, second and last coefficient of equation comparable with Eqn (1.47) must be positive, read after having introduced the radius of gyration k ($k^2 = I/m$):

$$b(k^2 + a^2)\Phi_1 + a(k^2 + b^2)\Phi_2 > 0 \tag{1.84}$$

$$\Phi_1 \Phi_2 \left(\frac{\partial \delta}{\partial l/R} \right)_V > 0 \tag{1.85}$$

The subscript V refers to the condition of differentiation with V kept constant, that is while staying on the speed line of Figure 1.17. The first condition (1.84) may be violated when we deal with tire characteristics showing a peak in side force and a downward sloping further part of the characteristic. The second condition corresponds to condition (1.65) for the linear model. Accordingly, instability is expected to occur beyond the point where the steer angle reaches a maximum while the speed is kept constant. This, obviously, can only occur in the oversteer range of operation. In the handling diagram the stability boundary can be assessed by finding the tangent to the handling curve that runs parallel to the speed line considered.

In the upper diagram of Figure 1.20 the stability boundary that holds for the right part of the diagram (a_y vs l/R) has been drawn for the system of Figure 1.17 that changes from initial understeer to oversteer. In the middle diagram, a number of shifted V-lines, each for a different steer angle δ, has been indicated. In each case, the points of intersection represent possible steady-state solutions. The highest point represents an unstable solution as the corresponding point on the speed line lies in the unstable area. When the steer angle is increased, the two points of intersections move toward each other. It turns out that for this type of handling curve, a range of δ values exists without intersections with the positive half of the curve. The fact that both right-hand turn solutions may vanish has serious implications which follow from the phase plot. At increased steer angle, however, new solutions may show up. At first, these solutions appear to be unstable, but at rather large steer angles of more than about 0.2 rad we find again stable solutions. These occur on the isolated branch where α_2 is small and α_1 is large. Apparently, we find that the vehicle that increases its speed while running at a constant turning radius will first cross the stability boundary and may then recover its stability by turning the steering wheel to a relatively large angle. In the diagram, the left part of the isolated branch is reached where stable spirals appear to occur. This phenomenon may correspond to similar experiences in the racing practice, cf. Jenkinson (1958).

The lower diagram depicts the handling curve for a car that remains understeered throughout the lateral acceleration range. Everywhere the steady-state cornering motion remains stable. Up to the maximum of the curve, the tangents slope to the left and cannot run parallel to a speed line. Beyond the peak, however, we can find a speed line parallel to the tangent, but at the same time one of the slopes (Φ_1) of the normalized axle characteristics starts to show a negative sign so that condition (1.85) is still satisfied. Similarly, the limit oversteer vehicle of the upper graph remains unstable beyond the peak. On the isolated part of the handling curve of the lower diagram, the motion remains unstable. It will be clear that the isolated branches vanish when we deal with axle characteristics that do not show a peak and decaying part of the curve.
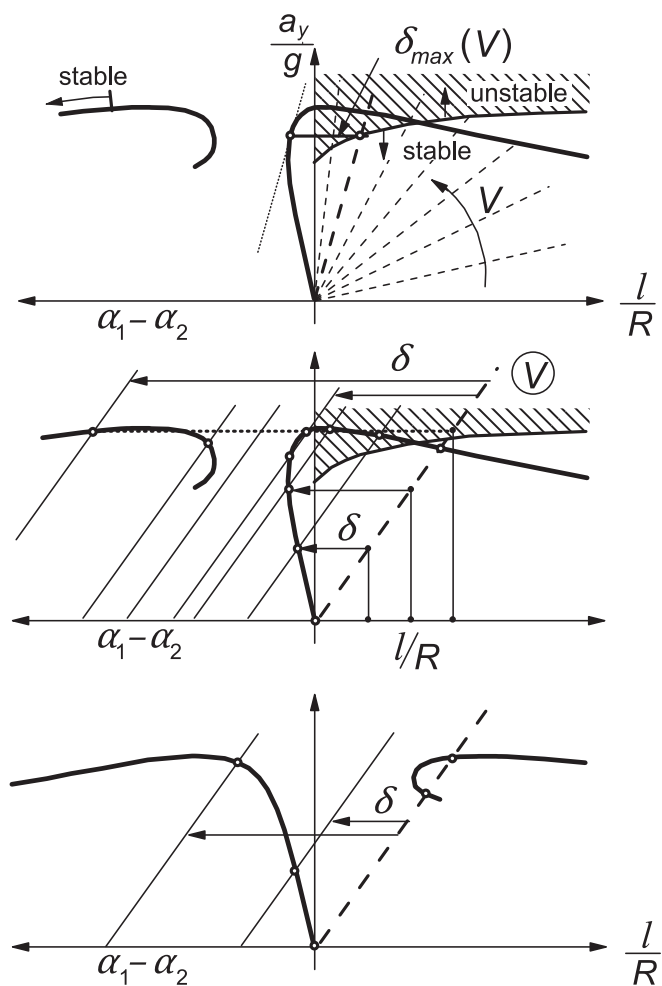
FIGURE 1.20 Construction of stability boundary (upper diagram, from Figure 1.17). On the isolated branch a stable range may occur (large steer angle as indicated in middle diagram). The lower diagram shows the case with complete understeer featuring a stable main branch.

It may seem that the establishment of unstable solutions has no particular value. It will become clear, however, that the existence and the location of both stable and unstable singular points play an important role in shaping the trajectories in the phase plane. Also, the nature of stability or instability in the singular points is of importance.

Exercise 1.3 Construction of the Complete Handling Diagram from Pairs of Axle Characteristics

We consider three sets of hypothetical axle characteristics (a, b, and c) shown in the graph of Figure 1.21. The dimensions of the vehicle model are: $a = b = \frac{1}{2}\, l = 1.5$ m.
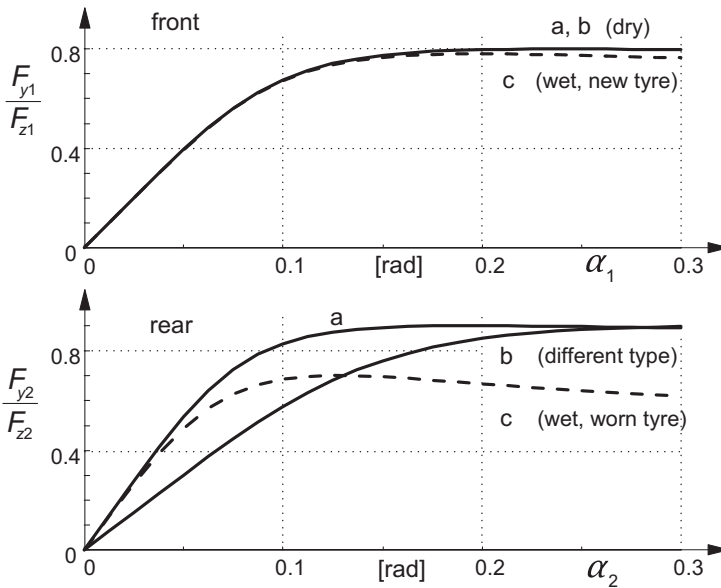
FIGURE 1.21   Three sets of hypothetical axle cornering characteristics (Exercise 1.3).

For the tires, we may employ axle characteristics described by the *magic formula* (1.6):

$$F_y = D \sin[C \arctan\{B\alpha - E(B\alpha - \arctan(B\alpha))\}]$$

We define the peak side force $D = \mu F_z$ and the cornering stiffness $C_{F\alpha} = BCD = c_{F\alpha}F_z$ so that $B = c_{F\alpha}/(C\mu)$. For the six tire/axle configurations, the parameter values have been given in the table below.

axle	case	μ	$c_{F\alpha}$	C	E
front	a,b	0.8	8	1.2	−2
	c	0.78	8	1.3	−2
rear	a	0.9	11	1.2	−2
	b	0.9	6	1.2	−2
	c	0.65	11	1.5	−1

Determine, for each of the three combinations (two dry, one wet),
1. The handling curve (cf. Figure 1.17).
2. The complete handling diagram (cf. Figure 1.17).
3. The portion of t curves where the vehicle shows an oversteer nature.

4. The stability boundary (associated with these oversteer ranges) in the (a_y/g versus l/R) diagram (= right-hand side of the handling diagram) (cf. Figure 1.20).
5. Indicate in the diagram (or in a separate graph):
    a. the course of the steer angle δ required to negotiate a curve with radius $R = 60$ m as a function of the speed V. If applicable, indicate the stability boundary, that is, the critical speed V_{crit}, belonging to this radius.
    b. the course of steer angle δ as a function of relative path curvature l/R at a fixed speed $V = 72$ km/h. If applicable, assess the critical radius R_{crit}.

For the vehicle systems considered so far, a unique handling curve appears to suffice to describe the steady-state turning behavior. Cases may occur, however, where more curves are needed, one for each velocity. A simple example is the situation when the car runs over a wet surface where the tire characteristics change considerably with speed. Also, as a result of the down forces acting on e.g., the body of a racing car, the tire loads increase with speed. Consequently, the tire characteristics change accordingly which requires an adaptation of the handling curve.

A more difficult and fundamentally different situation occurs when the vehicle is equipped with a third axle. Also in this case multiple handling curves arise. A tandem rear axle configuration of a heavy truck, for example, strongly opposes movement along a curved track. The slip angles of the two rear axles are different so that a counteracting torque arises. This torque gets larger when the turning radius becomes smaller. This may for instance occur at a given level of lateral acceleration. When at this level the speed becomes lower, the curvature must become larger and the opposing torque will increase which entails an increased front steer angle to generate a larger side force needed to balance the vehicle. This increased steer angle goes on top of the steer angle which was already larger because of the increased l/R. Here, l is the average wheel base. Consequently, in the handling diagram, the points on the handling curve belonging to the lower speed lie more to the left. For a detailed study on this special subject, we refer to Winkler (1998).

Assessment of the Influence of Pneumatic Trail on Handling Curve

So far the direct influence of the pneumatic trails has not been taken into account. As with the linear analysis, we may do this by considering the effective axle positions

$$a' = a - t_1, \quad b' = b + t_2 \quad \text{and} \quad l' = a' + b' \tag{1.86}$$

The difficulty we have to face now is the fact that these pneumatic trails t_i will vary with the respective slip angles. We have, if the residual torques are neglected,

$$t_i(\alpha_i) = -\frac{M_{zi}(\alpha_i)}{F_{yi}(\alpha_i)} \tag{1.87}$$

Introducing the effective axle loads

$$F'_{z1} = \frac{b'}{l'}mg, \quad F'_{z2} = \frac{a'}{l'}mg \tag{1.88}$$

yields for the lateral force balance instead of (1.80):

$$\frac{F_{y1}}{F'_{z1}} = \frac{F_{y2}}{F'_{z2}} = \frac{a_y}{g} \tag{1.89}$$

or after some rearrangements:

$$\frac{a'}{a}\frac{F_{y1}}{F_{z1}} = \frac{b'}{b}\frac{F_{y2}}{F_{z2}} = Q\frac{a_y}{g} \tag{1.90}$$

where

$$Q = \frac{l}{l'}\frac{a'b'}{ab} \approx 1 \tag{1.91}$$

The corrected normalized side force characteristics as indicated in (1.90) can be computed beforehand and drawn as functions of the slip angles, and the normal procedure to assess the handling curve can be followed. This can be done by taking the very good approximation $Q = 1$ or we might select a level of Qa_y/g and then assess the values of the slip angles that belong to that level of the corrected normalized side forces and compute Q according to (1.91) and from that the correct value of a_y/g.

Large Deviations with Respect to the Steady-State Motion

The variables r and v may be considered as the two state variables of the second-order nonlinear system represented by the Eqn (1.42). Through computer numerical integration, the response to a given arbitrary variation of the steer angle can be easily obtained. For motions with constant steer angle δ (possibly after a step change), the system is autonomous and the phase-plane representation may be used to find the solution. For that, we proceed by eliminating the time from Eqn (1.42). The result is a first-order nonlinear equation (using $k^2 = I/m$):

$$\frac{dv}{dr} = k^2\frac{F_{y1} + F_{y2} - mVr}{aF_{y1} - bF_{y2}} \tag{1.92}$$

Since F_{y1} and F_{y2} are functions of α_1 and α_2, it may be easier to take α_1 and α_2 as the state variables. With (1.44), we obtain

$$\frac{d\alpha_2}{d\alpha_1} = \frac{\dfrac{dv}{dr} - b}{\dfrac{dv}{dr} + a} \tag{1.93}$$

which becomes, with (1.92),

$$\frac{d\alpha_2}{d\alpha_1} = \frac{\dfrac{F_{y2}(\alpha_2)}{F_{z2}} - (\delta - \alpha_1 + \alpha_2)\dfrac{V^2}{gl}}{\dfrac{F_{y1}(\alpha_1)}{F_{z1}} - (\delta - \alpha_1 + \alpha_2)\dfrac{V^2}{gl}} \qquad (1.94)$$

For the sake of simplicity, we assumed $I/m = k^2 = ab$.

By using Eqn (1.94), the trajectories (solution curves) can be constructed in the (α_1, α_2) plane. The isocline method turns out to be straightforward and simple to employ. The pattern of the trajectories is strongly influenced by the so-called singular points. In these points the motion finds an equilibrium. In the singular points, the motion is stationary and consequently the differentials of the state variables vanish.

From the handling diagram, K/mg and l/R are readily obtained for given combinations of V and δ. Used in combination with the normalized tire characteristics F_{y1}/F_{z1} and F_{y2}/F_{z2}, the values of α_1 and α_2 are found, which form the coordinates of the singular points. The manner in which a stable turn is approached and from what collection of initial conditions such a motion can or cannot be attained may be studied in the phase plane. One of the more interesting results of such an investigation is the determination of the boundaries of the domain of attraction in case such a domain with finite dimensions exists. The size of the domain may give indications as to the so-called stability in the large. In other words, the question may be answered: does the vehicle return to its original steady-state condition after a disturbance and to what degree does this depend on the magnitude and point of application of the disturbance impulse?

For the construction of the trajectories, we draw isoclines in the (α_1, α_2) plane. These isoclines are governed by Eqn (1.94) with slope $d\alpha_2/d\alpha_1$ kept constant. The following three isoclines may already provide sufficient information to draw estimated courses of the trajectories. We have, for $k^2 = ab$,

vertical intercepts $(d\alpha_2/d\alpha_1 \to \infty)$:

$$\alpha_2 = \frac{gl}{V^2}\frac{F_{y1}(\alpha_1)}{F_{z1}} + \alpha_1 - \delta \qquad (1.95)$$

horizontal intercepts $(d\alpha_2/d\alpha_1 \to 0)$:

$$\alpha_1 = -\frac{gl}{V^2}\frac{F_{y2}(\alpha_2)}{F_{z2}} + \alpha_2 + \delta \qquad (1.96)$$

intercepts under 45° $(d\alpha_2/d\alpha_1 = 1)$:

$$\frac{F_{y1}(\alpha_1)}{F_{z1}} = \frac{F_{y2}(\alpha_2)}{F_{z2}} \qquad (1.97)$$

Figure 1.22 illustrates the way these isoclines are constructed. The system of Figure 1.17 with $k = a = b$, $\delta = 0.04$ rad, and $V = 50$ km/h has been considered. Note that the normalized tire characteristics appear in the left-hand diagram for the construction of the isoclines. The three points of intersection of the isoclines are the singular points. They correspond to the points I, II, and III of Figure 1.17. The stable point is a focus (spiral) point with a complex pair of solutions of the characteristic equation with a negative real part. The two unstable points are of the saddle type corresponding to a real pair of solutions, one of which is positive. The direction in which the motion follows the trajectories is still a question to be examined. Also for this purpose, the alternative set of axes with r and v as coordinates (multiplied with a factor) has been introduced in the diagram after using the relations (1.44).

From the original Eqn (1.42), it can be found that the isocline (1.97) forms the boundary between areas with $\dot{r} > 0$ and $\dot{r} < 0$ (indicated in Figure 1.22). Now it is easy to ascertain the direction along the trajectories. We note that the system exhibits a bounded domain of attraction. The boundaries are called separatrices. Once outside the domain, the motion finds itself in an unstable situation. If the disturbance remains limited in magnitude, so that resulting initial conditions of the state variables stay within the boundaries, then ultimately the steady-state condition is reached again.

For systems with normalized characteristics showing everywhere a positive slope, a handling curve arises that consists of only the main branch through the origin. If the rear axle characteristic (at least in the end) is higher than the front axle characteristic, the vehicle will show (at least in the limit) an understeer
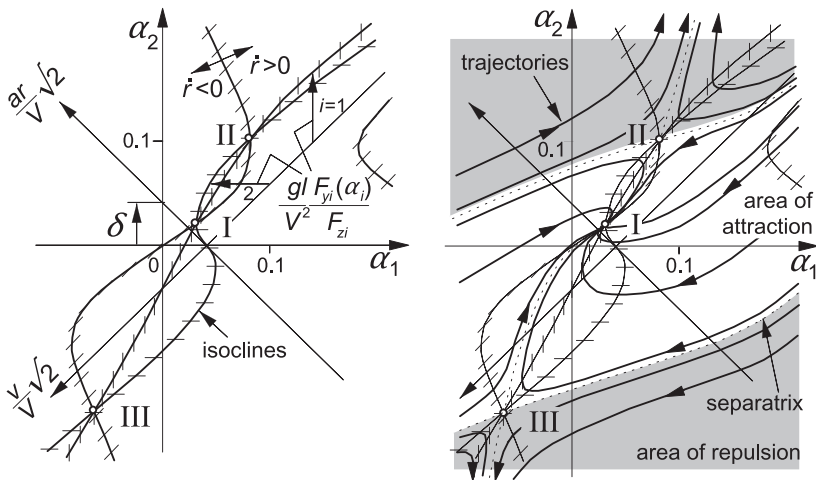

FIGURE 1.22 Isoclines for the construction of trajectories in the phase plane. Also shown: the three singular points I, II, and III (cf. Figure 1.17) and the separatrices constituting the boundary of the domain of attraction. Point I represents the stable cornering motion at steer angle δ.

nature and unstable singular points cannot occur. It will occur at least if in the case of initial oversteer the speed remains under the critical speed. In such cases, the domain of attraction is theoretically unbounded so that for all initial conditions ultimately the stable equilibrium is attained. The domain of Figure 1.22 appears to be open on two sides which means that initial conditions, in a certain range of (r/v) values, do not require to be limited in order to reach the stable point. Obviously, disturbance impulses acting in front of the center of gravity may give rise to such combinations of initial conditions.

In Figures 1.23 and 1.24, the influence of an increase in steer angle δ on the stability margin (distance between stable point and separatrix) has been shown for the two vehicles considered in Figure 1.20. The system of Figure 1.23 is clearly much more sensitive. An increase in δ (but also an increase in speed V) reduces the stability margin until it is totally vanished as soon as the two singular points merge (also the corresponding points I and II on the handling curve of Figure 1.17) and the domain breaks open. As a result, all trajectories starting above the lower separatrix tend to leave the area. This can only be
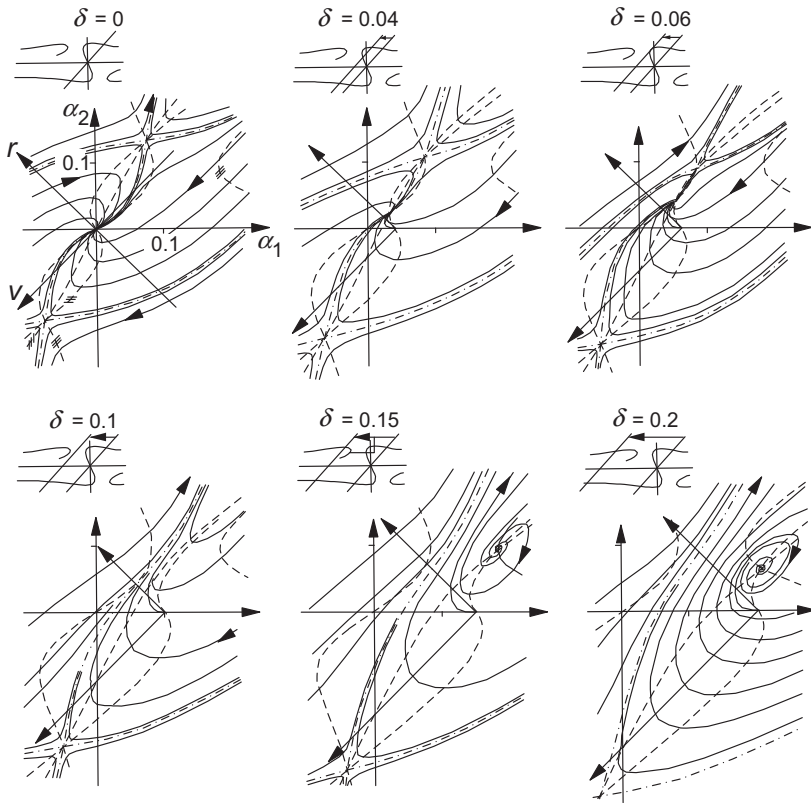

FIGURE 1.23   Influence of steering on the stability margin (system of Figure 1.20 (top)).
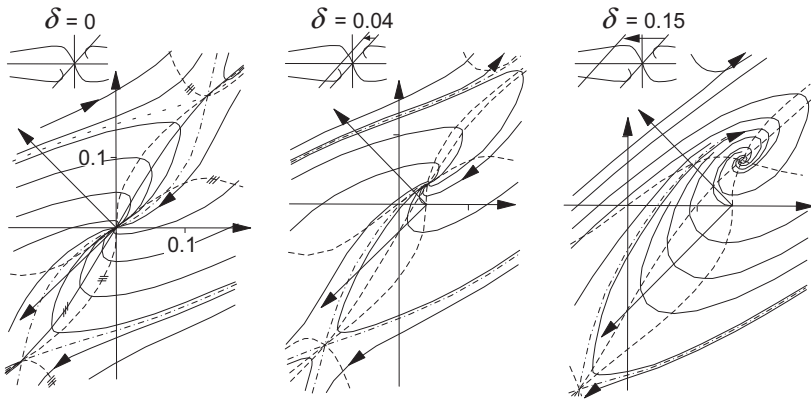
FIGURE 1.24 Influence of steering on the stability margin (system of Figure 1.20 (bottom)).

stopped by either quickly reducing the steer angle or enlarging δ to around 0.2 rad or more. The latter situation appears to be stable again (focus) as has been stated before. For the understeered vehicle of Figure 1.24, stability is practically always ensured.

For a further appreciation of the phase diagram, it is of interest to determine the new initial state (r_o, v_o) after the action of a lateral impulse to the vehicle (cf. Figure 1.25). For an impulse S acting at a distance x in front of the center of gravity, the increase in r and v becomes
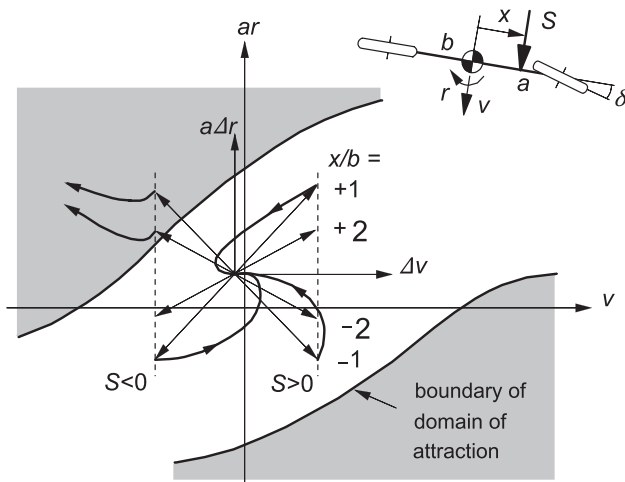

FIGURE 1.25 Large disturbance in a curve. New initial state vector $(\Delta v, \Delta r)$ after the action of a lateral impulse S. Once outside the domain of attraction, the motion becomes unstable and may get out of control.

$$\Delta r = \frac{Sx}{l}, \quad \Delta v = \frac{S}{m} \tag{1.98}$$

which results in the direction

$$\frac{a\Delta r}{\Delta v} = \frac{x}{b}\frac{ab}{k^2} \tag{1.99}$$

The figure shows the change in state vector for different points of application and direction of the impulse S ($k^2 = I/m = ab$). Evidently, an impulse acting at the rear (in outward direction) constitutes the most dangerous disturbance. On the other hand, an impulse acting in front of the center of gravity about half way from the front axle does not appear to be able to get the new starting point outside of the domain of attraction irrespective of the intensity of the impulse.

When the slip angles become larger, the forward speed u may no longer be considered as a constant quantity. Then, the system is described by a third-order set of equations. In the paper (Pacejka 1986), the solutions for the simple automobile model have been presented also for yaw angles $> 90°$.

1.3.4. The Vehicle at Braking or Driving

When the vehicle is subjected to longitudinal forces that may result from braking or driving actions possibly to compensate for longitudinal wind drag forces or down or upward slopes, fore-and-aft load transfer will arise (Figure 1.26). The resulting change in tire normal loads causes the cornering stiffnesses and the peak side forces of the front and rear axles to change. Since, as we assume here, the fore-and-aft position of the center of gravity is not affected (no relative car body motion), we may expect a change in handling behavior indicated by a rise or drop of the understeer gradient. In addition, the
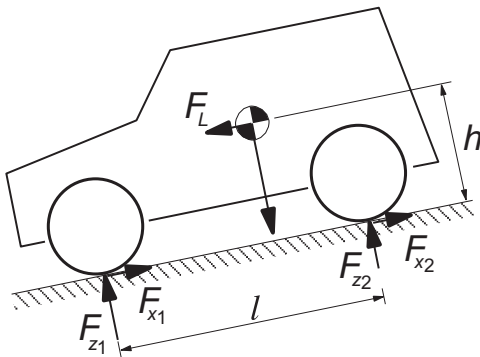

FIGURE 1.26 The automobile subjected to longitudinal forces and the resulting load transfer.

longitudinal driving or braking forces give rise to a state of combined slip, thereby affecting the side force in a way as shown in Figure 1.2.

For moderate driving or braking forces, the influence of these forces on the side force F_y is relatively small and may be neglected for this occasion. This means that, for now, the cornering stiffness may be considered to be dependent on the normal load only. The upper-left diagram of Figure 1.3 depicts typical variations of the cornering stiffness with vertical load.

The load transfer from the rear axle to the front axle that results from a forward longitudinal force F_L acting at the center of gravity at a height h above the road surface (F_L possibly corresponding to the inertial force at braking) becomes

$$\Delta F_z = \frac{h}{l} F_L \qquad (1.100)$$

The understeer gradient reads according to Eqn (1.60):

$$\eta = \frac{F_{z1o}}{C_1(F_{z1})} - \frac{F_{z2o}}{C_2(F_{z2})} \qquad (1.101)$$

The static axle loads F_{zio} ($i = 1$ or 2) are calculated according to Eqn (1.59), while the actual loads F_{zi} front and rear become

$$F_{z1} = F_{z1o} + \Delta F_z, \quad F_{z2} = F_{z2o} - \Delta F_z \qquad (1.102)$$

At moderate braking with deceleration $-a_x = F_L/m$, the load transfer remains small and we may use the linearized approximation of the variation of cornering stiffness with vertical load:

$$C_i = C_{io} + \zeta_{\alpha i} \Delta F_{zi} \text{ with } \zeta_{\alpha i} = \left(\frac{\partial C_i}{\partial F_{zi}} \right)_{F_{zio}} \qquad (1.103)$$

The understeer gradient (1.101) can now be expressed in terms of the longitudinal acceleration a_x (which might be minus the forward component of the acceleration due to gravity parallel to the road). We obtain

$$\eta = \eta_o + \lambda \frac{a_x}{g} \qquad (1.104)$$

with the determining factor λ approximately expressed as

$$\lambda = \zeta_{\alpha 1} \frac{h}{b} \left(\frac{F_{z1o}}{C_{1o}} \right)^2 + \zeta_{\alpha 2} \frac{h}{a} \left(\frac{F_{z2o}}{C_{2o}} \right)^2 \qquad (1.105)$$

and η_o denoting the original value not including the effect of longitudinal forces. Obviously, since $\zeta_{\alpha 1,2}$ is usually positive, negative longitudinal accelerations a_x, corresponding to braking, will result in a decrease of the degree of understeer.

To illustrate the magnitude of the effect, we use the parameter values given in Table 1.1 (p. 34) and add the c.g. height $h = 0.6$ m and the cornering stiffness versus load gradients $\zeta_{\alpha i} = 0.5 C_{io}/F_{zio}$. The resulting factor appears to take the value $\lambda = 0.052$. This constitutes an increase of η equal to $0.052 a_x/g$. Apparently, the effect of a_x on the understeer gradient is considerable when regarding the original value $\eta_o = 0.0174$.

As illustrated by Figure 1.9, the peak side force will be diminished if a longitudinal driving or braking force is transmitted by the tire. This will have an impact on the resulting handling diagram in the higher range of lateral acceleration. The resulting situation may be represented by the second and third diagrams of Figure 1.18 corresponding to braking (or driving) at the front or rear respectively. The problem becomes considerably more complex when we realize that at the front wheels, the components of the longitudinal forces perpendicular to the x-axis of the vehicle are to be taken into account. Obviously, we find that at braking of the front wheels, these components will counteract the cornering effect of the side forces and thus will make the car more understeer. The opposite occurs when these wheels are driven (more oversteer). For a more elaborate discussion on this item, we may refer to Pacejka (1973b).

At hard braking, possibly up to wheel lock, stability and steerability may deteriorate severely. This more complex situation will be discussed in Chapter 3 where more information on the behavior of tires at combined slip is given.

1.3.5. The Moment Method

Possible steady-state cornering conditions, stable or unstable, have been portrayed in the handling diagram of Figure 1.17. In Figure 1.22, motions tending to or departing from these steady-state conditions have been depicted. These motions are considered to occur after a sudden change in steer angle. The potential available to deviate from the steady turn depends on the margin of the front and rear side forces to increase in magnitude. For each point on the handling curve, it is possible to assess the degree of maneuverability in terms of the moment that can be generated by the tire side forces about the vehicle's center of gravity. Note that at the steady-state equilibrium condition, the tire side forces are balanced with the centrifugal force and the moment equals zero.

In general, the handling curve holds for a given speed of travel. That is so, when e.g., the aerodynamic down forces are essential in the analysis. In Figure 1.27 a diagram has been presented that is designated as the *MMM* diagram (the Milliken moment method diagram) and is computed for a speed of 60 mph. The force–moment concept was originally proposed by W.F. Milliken in 1952 and thereafter continuously further developed by the Cornell Aeronautical Laboratory staff and by Milliken research associates. A detailed description is given in Milliken's book (1995).
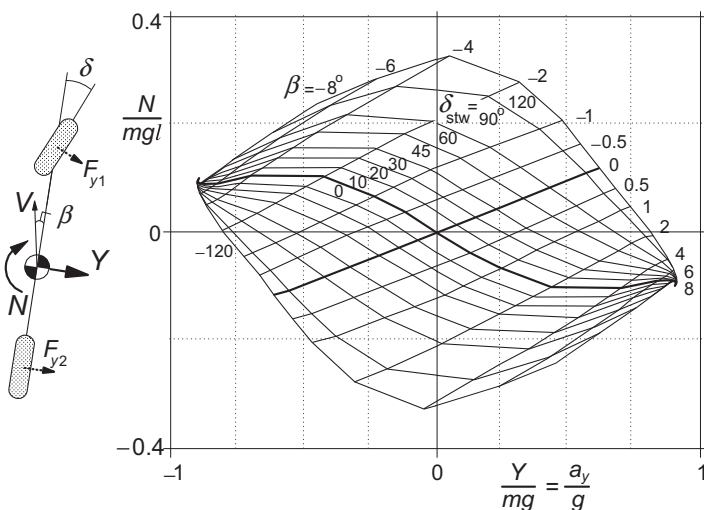
FIGURE 1.27 The *MMM* diagram portraying the car's potential maneuvering capacity.

The graph shows curves of the resulting tire moment N vs the resulting tire side force Y in nondimensional form. The resulting force and moment result from the individual side forces and act from ground to vehicle. For greater accuracy, one may take the effect of the pneumatic trails into consideration. Two sets of curves have been plotted: one set for constant values of the vehicle side slip angle β with the steering wheel angle δ_{stw} as parameter and the other set for constant steer angle and varying slip angle. Along the horizontal axis, the moment is zero and we have the steady-state equilibrium cornering situation that corresponds to the handling curve. It is observed that for the constant speed considered in the diagram, the steer angle increases when the total side force Y or lateral acceleration a_y is chosen larger which indicates that the motion remains stable. At the limit (near number 2), the maximum steady-state lateral acceleration is attained. At that point, the ability to generate a positive moment is exhausted. Only a negative moment may still be developed by the car that tends to straighten the curve that is being negotiated. As we have seen in Figure 1.18, second diagram, there is still some side force margin at the rear tire which can be used to increase the lateral acceleration in a transient fashion. At the same time, however, the car yaws outward because the associated moment is negative (cf. Figure 1.27, the curve near number 8). How to get at points below the equilibrium point near the number 2 is a problem. Rear wheel steering is an obvious theoretical option. In that way, the vehicle slip angle β and front steer angle δ can remain unchanged while the rear steer angle produces the desired rear tire slip angle.

Of course, the diagram needs to be adapted in the case of rear wheel steering. Another more practical solution would be to bring the vehicle in the

desired attitude ($\beta \rightarrow 8°$) by briefly inducing large brake or drive slip at the rear that lowers the cornering force and lets the car swing to the desired slip angle while at the same time the steering wheel is turned backward to even negative values.

The *MMM* diagram, which is actually a Gough plot (for a single tire, cf. Figures 3.5 and 3.29) established for the whole car at different steer angles, may be assessed experimentally through either outdoor or indoor experiments. On the proving ground, a vehicle may be attached at the side of a heavy truck or railway vehicle and set at different slip angles while the force and moment are being measured (tethered testing), cf. Milliken (1995). Figure 1.28 depicts the remarkable laboratory MMM test machine. This MTS Flat-Trac Roadway Simulator™ uses four flat belts which can be steered and driven independently. The car is constrained in its center of gravity but is free to roll and pitch.

1.3.6. The Car-Trailer Combination

In this section we will discuss the role of the tire in connection with the dynamic behavior of a car that tows a trailer. More specifically, we will study the possible unstable motions that may show up with such a combination. Linear differential equations are sufficient to analyze the stability of the straight-ahead motion. We will again employ Lagrange's equations to set up the equations of motion. The original Eqn (1.25) may be employed because the yaw angle is assumed to remain small. The generalized coordinates Y, ψ, and θ are used to describe the car's lateral position and the yaw angles of car and
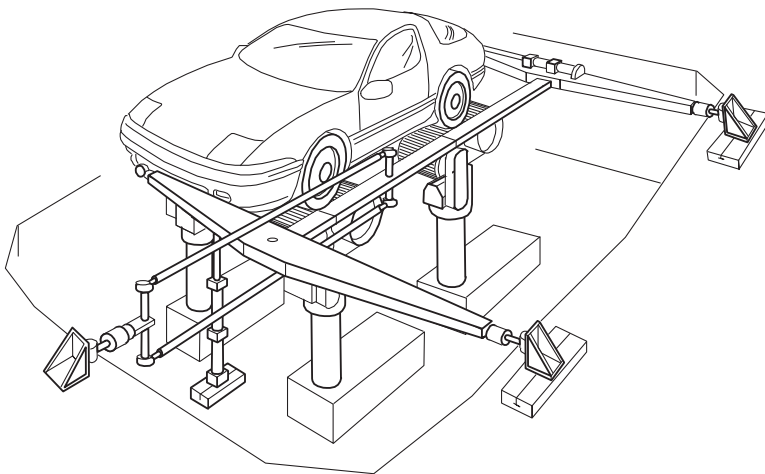

FIGURE 1.28 The MTS Flat-Trac Roadway Simulator™, Milliken (1995).

trailer respectively. The forward speed dX/dt ($\approx V \approx u$) is considered to be constant. Figure 1.29 gives a top view of the system with three degrees of freedom. The alternative set of three variables v, r, the articulation angle φ, and the vehicle velocity V (a parameter) which are not connected to the inertial axes system (O, X, Y) has been indicated as well and will be employed later on. The kinetic energy for this system becomes, if we neglect all the terms of the second order of magnitude (products of variables),

$$T = \frac{1}{2}m(\dot{X}^2 + \dot{Y}^2) + \frac{1}{2}I\dot{\psi}^2 + \frac{1}{2}m_c\left\{\dot{X}^2 + (\dot{Y} - h\dot{\psi} - f\dot{\theta})^2\right\} + \frac{1}{2}I_c\dot{\theta}^2 \quad (1.106)$$

The potential energy remains zero:

$$U = 0 \qquad (1.107)$$

and the virtual work done by the external road contact forces acting on the three axles reads

$$\delta W = F_{y1}\delta(Y + a\psi) + F_{y2}\delta(Y - b\psi) + F_{y3}\delta(Y - h\psi - g\theta) \qquad (1.108)$$

With the use of Eqns (1.25) and (1.29), the following equations of motion are established for the generalized coordinates Y, ψ, and θ:

$$(m + m_c)\ddot{Y} - m_c(h\ddot{\psi} + f\ddot{\theta}) = F_{y1} + F_{y2} + F_{y3} \qquad (1.109)$$

$$(I_c + m_c f^2)\ddot{\theta} - m_c f(\ddot{Y} - h\ddot{\psi}) = -gF_{y3} \qquad (1.110)$$

$$(I + m_c h^2)\ddot{\psi} - m_c h(\ddot{Y} - f\ddot{\theta}) = aF_{y1} - bF_{y2} - hF_{y3} \qquad (1.111)$$

This constitutes a system of the sixth order. By introducing the velocities v and r, the order can be reduced to four. In addition, the angle of articulation φ will be used. We have the relations
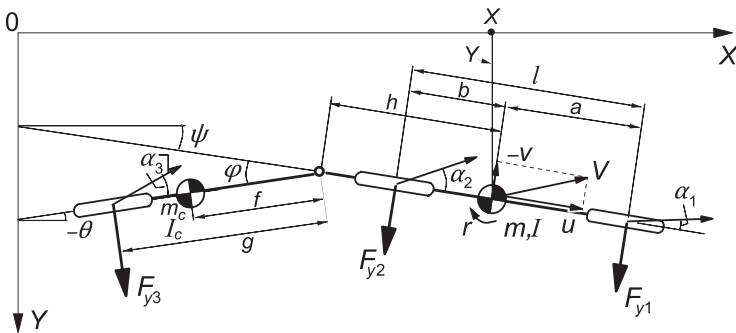
$$\dot{Y} = V\psi + v, \quad \dot{\psi} = r, \quad \theta = \psi - \varphi \qquad (1.112)$$

FIGURE 1.29   Single track model of car-trailer combination.

And, with these the equations for v, r, and φ,

$$(m + m_c)(\dot{v} + Vr) - m_c\{(h + f)\dot{r} - f\ddot{\varphi}\} = F_{y1} + F_{y2} + F_{y3} \tag{1.113}$$

$$\{I + m_ch(h + f)\}\dot{r} - m_ch(\dot{v} + Vr + f\ddot{\varphi}) = aF_{y1} - bF_{y2} - hF_{y3} \tag{1.114}$$

$$(I_c + m_cf^2)(\ddot{\varphi} - \dot{r}) + m_cf(\dot{v} + Vr - h\dot{r}) = gF_{y3} \tag{1.115}$$

The right-hand members are still to be expressed in terms of the motion variables. With the axle cornering stiffnesses C_1, C_2, and C_3, we have

$$
\begin{aligned}
F_{y1} &= C_1\alpha_1 = -C_1\frac{v + ar}{V} \\
F_{y2} &= C_2\alpha_2 = -C_2\frac{v - br}{V} \\
F_{y3} &= C_3\alpha_3 = -C_3\left(\frac{v - hr - g(r - \dot{\varphi})}{V} + \varphi\right)
\end{aligned}
\tag{1.116}
$$

From the resulting set of linear differential equations, the characteristic equation may be derived which is of the fourth degree. Its general structure is

$$a_0s^4 + a_1s^3 + a_2s^2 + a_3s + a_4 = 0 \tag{1.117}$$

The stability of the system can be investigated by considering the real parts of the roots of this equation or we might employ the criterion for stability according to Routh-Hurwitz. According to this criterion, the system of order n is stable when all the coefficients a_i are positive and the Hurwitz determinants H_{n-1}, H_{n-3} etc. are positive. For our fourth-order system, the complete criterion for stability reads

$$H_3 = \begin{bmatrix} a_1 & a_0 & 0 \\ a_3 & a_2 & a_1 \\ 0 & a_4 & a_3 \end{bmatrix} = a_1a_2a_3 - a_1^2a_4 - a_0a_3^2 > 0 \tag{1.118}$$

$$a_i > 0 \quad \text{for } i = 0, 1, \dots 4$$

In Figure 1.30, the boundaries of stability have been presented in the caravan axle cornering stiffness vs speed parameter plane. The three curves belong to the three different sets of parameters for the position f of the caravan's center of gravity and the caravan's mass m_c as indicated in the figure. An important result is that a lower cornering stiffness promotes oscillatory instability: the critical speed beyond which instability occurs decreases. Furthermore, it appears from the diagram that moving the caravan's center of gravity forward (f smaller) stabilizes the system which is reflected by the larger critical speed. A heavier caravan (m_c larger) appears to be bad for stability. Furthermore, it has been found that a larger draw bar length g is favorable for stability.
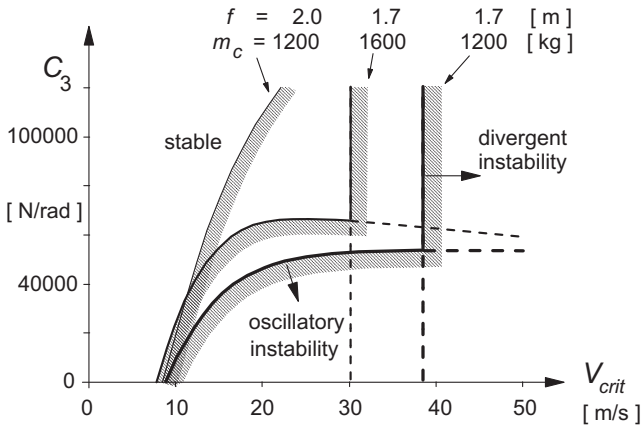
FIGURE 1.30 Stability boundaries for the car caravan combination in the caravan cornering stiffness vs critical speed diagram. Vehicle parameters according to Table 1.1, in addition: $h = 2$ m, $g = 2$ m, $k_c = 1.5$ m ($I_c = m_c k_c^2$), cf. Figure 1.29.

It turns out that a second type of instability may show up. This occurs when the portion of the weight of the caravan supported by the coupling point becomes too large. This extra weight is felt by the towing vehicle and makes it more oversteer. The critical speed associated with this phenomenon is indicated in the diagram by the vertical lines. This divergent instability occurs when (starting out from a stable condition) the last coefficient becomes negative, that is, $a_n = a_4 < 0$.

The oscillatory instability connected with the 'snaking' phenomenon arises as soon as (from a stable condition) the second highest Hurwitz determinant becomes negative, $H_{n-1} = H_3 < 0$ (then also $H_n < 0$), cf. Klotter (1960) or Leipholz (1987). When the critical speed is surpassed, self-excited oscillations are created which shows an amplitude that, in the actual nonlinear case, does not appear to limit itself. This is in contrast to the case of the wheel shimmy phenomenon to be treated in Chapter 5 where a stable limited oscillation appears to arise. The cause of the unlimited snaking oscillation is that with increasing amplitudes also the slip angle increases which lowers the average cornering stiffness as a consequence of the degressively nonlinear cornering force characteristic. From the diagram we found that this will make the situation increasingly worse. As has been seen from full vehicle/caravan model simulations, the whole combination will finally overturn. Another effect of this reduction of the average cornering stiffness is that when the vehicle moves at a speed lower than the critical speed, the originally stable straight-ahead motion may become unstable if, through the action of an external disturbance (side wind gust), the slip angle of the caravan axle becomes too large (surpassing of the associated unstable limit cycle). This is an unfortunate, possibly dangerous situation! We refer to Troger and Zeman (1984) for further details.

Exercise 1.4 Stability of a Trailer

Consider the trailer of Figure 1.31 that is towed by a heavy steadily moving vehicle at a forward speed V along a straight line. The trailer is connected to the vehicle by means of a hinge. The attachment point shows a lateral flexibility that is represented by the lateral spring with stiffness c_y. Furthermore, a yaw torsional spring and damper are provided with coefficients c_φ and k_φ.

Derive the equations of motion of this system with generalized coordinates y and φ. Assume small displacements so that the equations can be kept linear. The damping couple $k_\varphi \dot{\varphi}$ may be considered as an external moment acting on the trailer or we may use the dissipation function $D = (1/2)k_\varphi \dot{\varphi}^2$ and add $+\partial D/\partial \dot{q}_i$ to the left-hand side of Lagrange's Eqn (1.25). Obviously, the introduction of this extra term will be beneficial particularly when the system to be modeled is more complex.

Assess the condition for stability for this fourth-order system. Simplify the system by putting $g = f$ and $c_\varphi = k_\varphi = 0$. Now find the explicit conditional statement for the cornering stiffness C.
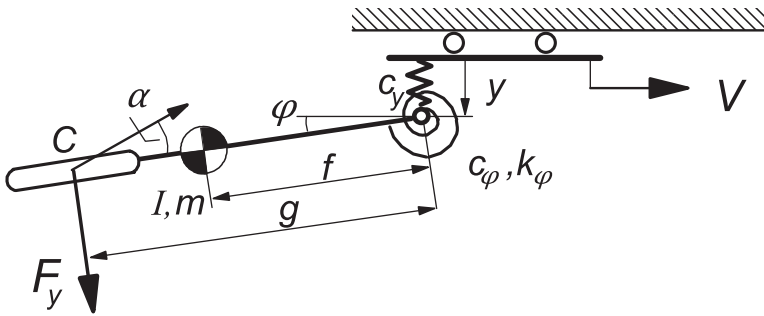

FIGURE 1.31 On the stability of a trailer (Exercise 1.4).

1.3.7. Vehicle Dynamics at More Complex Tire Slip Conditions

So far, relatively simple vehicle dynamics problems have been studied in which the basic steady-state cornering force versus slip angle characteristic plays the dominant role. The situation becomes more complex when matters like combined slip at hard braking, wheel camber, tire transient and vibrational properties, and e.g., obstacle crossings are to be considered.

In the subsequent chapters, tire performance and modeling will be treated in greater detail which enables us to introduce relevant tire properties in the analysis. The following specific subjects will be studied as applications of the tire modeling theory:

- Vehicle stability at excessive braking and wheel lock (Chapter 3)
- Motorcycle steady-state cornering (Chapter 11)

- Wheel shimmy (Chapter 6)
- Steering vibrations (Chapter 8)
- Motorcycle weave and wobble (Chapter 11)
- Tire out-of-roundness (Chapter 8)
- Cornering on uneven roads (Chapters 5,8)
- ABS on uneven roads (Chapter 8)
- Traversing short obstacles (Chapter 10)
- Parking (Chapter 9)

Online, cf. App. 2, several types of car handling experiments are discussed and compared with theoretical results of Sec. 1.3.2. *MATLAB* programs are presented, also for the three degree of freedom model, for the benefit of the interested reader.